

AD-A127 926

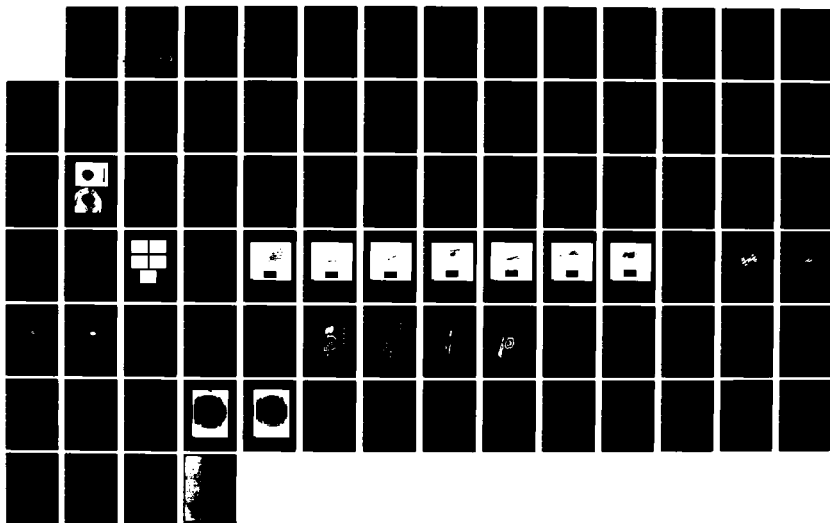
PULSED LASER DEVICE DEVELOPMENT PROGRAM VOLUME IV ABEL  
II (AIR-BREATHING) (U) AVCO EVERETT RESEARCH LAB INC  
EVERETT MA M J SMITH MAY 81 DARH01-80-C-0208

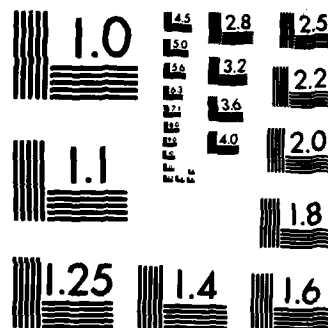
1/1

UNCLASSIFIED

F/G 28/5

NL





MICROCOPY RESOLUTION TEST CHART  
NATIONAL BUREAU OF STANDARDS-1963-A

**A 127926**

(13)

**PULSED LASER DEVICE DEVELOPMENT PROGRAM**

**VOLUME IV OF IV**

**ABEL II PRELIMINARY BEAM QUALITY TEST REPORT**

**M.J. Smith**

**AVCO EVERETT RESEARCH LABORATORY, INC.**  
a Subsidiary of the Avco Corporation  
2385 Revere Beach Parkway  
Everett, Massachusetts 02149

**May 1981**

**Final Technical Report**  
**31 December 1979 - 30 September 1981**

APPROVED FOR PUBLIC RELEASE; DISTRIBUTION UNLIMITED.

prepared for

**HEADQUARTERS**  
**U.S. ARMY MISSILE COMMAND**  
**Redstone Arsenal, Alabama 35809**

DTIC FILE COPY

DTIC  
ELECTRONIC  
MAY 10 1983  
A

"Original contains color  
plates: All DTIC reproductions  
will be in black and  
white"

83 05 09-143

UNCLASSIFIED

SECURITY CLASSIFICATION OF THIS PAGE (When Data Entered)

REPORT DOCUMENTATION PAGE		READ INSTRUCTIONS BEFORE COMPLETING FORM								
1. REPORT NUMBER	2. GOVT ACCESSION NO. <b>AD-A127926</b>	3. RECIPIENT'S CATALOG NUMBER								
4. TITLE (and Subtitle) <b>Pulsed Laser Device Development Program - Volume IV of IV ABEL II Preliminary Beam Quality Test Report</b>		5. TYPE OF REPORT & PERIOD COVERED <b>Final Technical Report for Period 12/31/79-9/30/81</b>								
7. AUTHOR(s) <b>M.J. Smith</b>		6. PERFORMING ORG. REPORT NUMBER								
9. PERFORMING ORGANIZATION NAME AND ADDRESS <b>Avco Everett Research Laboratory, Inc. a Subsidiary of Avco Corporation 2385 Revere Beach Parkway Everett, Massachusetts 02149</b>		8. CONTRACT OR GRANT NUMBER(s) <b>DAAH01-80-C-0208</b>								
11. CONTROLLING OFFICE NAME AND ADDRESS <b>Headquarters U.S. Army Missile Command Redstone Arsenal, Alabama 35809</b>		10. PROGRAM ELEMENT, PROJECT, TASK AREA & WORK UNIT NUMBERS <b>CDRL Item A008</b>								
14. MONITORING AGENCY NAME & ADDRESS (if different from Controlling Office)		12. REPORT DATE <b>May 1981</b>								
		13. NUMBER OF PAGES <b>89</b>								
		15. SECURITY CLASS. (of this report) <b>Unclassified</b>								
		15a. DECLASSIFICATION/DOWNGRADING SCHEDULE								
16. DISTRIBUTION STATEMENT (of this Report) <b>Approved for Public Release; Distribution Unlimited</b>										
17. DISTRIBUTION STATEMENT (of the abstract entered in Block 20, if different from Report)										
18. SUPPLEMENTARY NOTES										
19. KEY WORDS (Continue on reverse side if necessary and identify by block number)										
<table border="0"> <tr> <td>Electric Discharge Laser</td> <td>Infrared Photography</td> </tr> <tr> <td>Repetitively Pulsed</td> <td>Aberrations</td> </tr> <tr> <td>Beam Quality</td> <td>Near Diffraction Limited</td> </tr> <tr> <td>Beam Diagnostic</td> <td>Optical Characterization</td> </tr> </table>			Electric Discharge Laser	Infrared Photography	Repetitively Pulsed	Aberrations	Beam Quality	Near Diffraction Limited	Beam Diagnostic	Optical Characterization
Electric Discharge Laser	Infrared Photography									
Repetitively Pulsed	Aberrations									
Beam Quality	Near Diffraction Limited									
Beam Diagnostic	Optical Characterization									
20. ABSTRACT (Continue on reverse side if necessary and identify by block number)										
<p>Single-pulse beam quality was measured on the ABEL laser, for output energies in the 2.0-2.8 kJ range. No device adjustments or modifications to optimize beam quality were undertaken.</p> <p>Quantities measured were near-field intensity and total energy, farfield intensity and total energy, and fluence distribution in the focal spot region. This last measurement utilized</p>										

UNCLASSIFIED

SECURITY CLASSIFICATION OF THIS PAGE(When Data Entered)

20.

pulsed IR photography, a new and promising technique. Comparison cavity interferograms were also taken.

Energy delivery from near-field to farfield was 60-65%, and was not dependent on laser output energy, flow rate, or resonator configuration. The intensity measurements showed a tendency for farfield intensity at the end of the optical pulse to decay sooner than that of the near-field.

Beam quality, as measured by fraction of farfield energy within the first Airy disc, was equal to or less than 1.25 times diffraction limited for four shots analyzed in detail. Astigmatism was the largest contributor to the observed focal spot distortion.

Cavity interferometry results predicted beam quality of 1.15 times diffraction limited. The astigmatism evident in the focal spots did not appear in the interferograms; its source is unclear at the time of this reporting.

UNCLASSIFIED

SECURITY CLASSIFICATION OF THIS PAGE(When Data Entered)

## SUMMARY OF REPORT VOLUMES

This document is one of four volumes which, collectively, comprise the Final Technical Report for the Pulsed Laser Device Development Program, also known as ABEL II (ABEL is an acronym for Air-Breathing Electric Laser). Volume I delineates the contract technology development effort on a by-task basis and references the three major experimental activities described separately in Volumes II, III and IV.

- Volume I - ABEL II Technology (Confidential)
- Volume II - ABEL II Average Power/Low Power Test Report (Confidential)
- Volume III - ABEL II Small-Scale Flow Test Report (Unclassified)
- Volume IV - ABEL II Preliminary Beam Quality Test Report (Unclassified)



# ACKNOWLEDGMENT

We wish to thank the U.S. Air Force Weapons Laboratory for assistance in interferogram reduction.

## TABLE OF CONTENTS

<u>Section</u>	<u>Page</u>
Summary of Report Volumes	1
Acknowledgments	2
List of Illustrations	5
1.0 INTRODUCTION	9
1.1 Experimental Objectives	9
2.0 EXPERIMENTAL METHOD	11
2.1 Concept of Diagnostic	11
2.1.1 Previous Techniques	11
2.1.2 Diagnostic Concept Used for ABEL Preliminary Beam Quality	13
2.2 Experimental Setup	13
2.2.1 General	13
2.2.2 Attenuator Screens	15
2.2.3 Farfield Diagnostic	16
2.2.4 I(t) Detectors	20
2.2.5 Near-Field Diagnostic	20
2.2.6 Near-Field Energy	23
2.3 10.6 $\mu$ m Photography	24
2.4 Interferometry Setup	24
3.0 TEST DESCRIPTION	31
4.0 TEST DATA	33
4.1 Farfield/Near-Field Energy Comparison	33
4.1.1 Experimental Issue	33
4.1.2 Test Data	33
4.1.3 Possible Explanations	35
4.2 Farfield/Near-Field Time-Resolved Intensity	40
4.2.1 Experimental Issue	40
4.2.2 Data	42
4.2.3 Discussion	42



<u>Section</u>	<u>Page</u>
4.3 Specimen 10.6 $\mu$ m IR Photographs	44
4.3.1 Experimental Issue	44
4.3.2 Data	44
4.3.3 Discussion	44
4.4 Beam Quality Calculations	57
4.4.1 Experimental Issue	57
4.4.2 Data	59
4.4.3 Discussion	69
4.5 Interferometry Results	73
4.5.1 Experimental Issue	73
4.5.2 Data	75
4.5.3 Discussion	76
5.0 CONCLUSIONS AND SUMMARY	81
 <u>Appendices</u>	
A Theoretical Focal Spot Patterns	A-1
B Comparison of Times-Diffraction-Limited Numbers for Beams with Astigmatism	B-1

## LIST OF ILLUSTRATIONS

<u>Figure</u>		<u>Page</u>
1	Basic "Power-in-the Bucket" Scheme for Laser Beam	12
2	Room Layout for ABEL Preliminary Beam Quality Measurements	14
3	Farfield Schematic	17
4	Geometry for Estimating Salt Beamsplitter Placement	19
5	Shielding Arrangement for Molelectron Pyroelectric Detectors	21
6	Near-Field Schematic	22
7	Infrared Photography with Silver Halide Film	25
8	Infrared Film Calibration Curve for ABEL Measurements	26
9	Focal Spot Infrared Photography of CO <sub>2</sub> Pulsed Electric Discharge Laser Farfield Beam	27
10	Interferometry Diagnostic for ABEL	30
11	Resonator Configuration Used for Beam Quality Tests	32
12	Farfield Energy Delivery Ratio vs Near-Field Energy	34
13	Typical Intensity Profile of Pulsed CO <sub>2</sub> Laser Beam	37
14	Turbulence Scale Size and Measured Energy Delivery Ratio	41
15	Near-Field and Farfield I(t) Traces for 30 January 1981	43
16	Focal Spot Infrared Photograph for Shot #11, 30 January 1981	45
17	Focal Spot Infrared Photograph for Shot #4, 29 January 1981	46

<u>Figure</u>		<u>Page</u>
18	Focal Spot Infrared Photograph for Shot #2, 30 January 1981	47
19	Focal Spot Infrared Photograph for Shot #4, 2 February 1981	48
20	Focal Spot Infrared Photograph for Shot #13, 31 January 1981	49
21	Focal Spot Infrared Photograph for Shot #3, 2 February 1981	50
22	Focal Spot Infrared Photograph for Shot #7, 2 February 1981	51
23	Calculated Focal Spot Intensity Contours for Astigmatism with Axes at 45° to Resonator Axes; Aberration Strength = 0.272 Waves RMS	53
24	Calculated Focal Spot Intensity Contours for Astigmatism with Axes at 45° to Resonator Axes; Aberration Strength = 0.174 Waves RMS	54
25	Calculated Focal Spot Intensity Contours for Astigmatism with Axes at 45° to Resonator Axes; Aberration Strength = 0.116 Waves RMS	55
26	Calculated Focal Spot Intensity Contours for Perfect Beam; Compare to Figures 23 through 25	56
27	Fluence Map of ABEL Focal Spot	61
28	Fluence Map of ABEL Focal Spot (the Shading at Left is a Background Artifact)	63
29	Fluence Map of ABEL Focal Spot	65
30	Fluence Map of ABEL Focal Spot	67
31	Rectangular Near-Field	70
32	Theoretical Encircled Energy Ratios for the Various Resonator Configurations	72
33	Full-System ABEL Cavity Interferogram (No Energy Loading); Calculated $I/I_0 = 0.76$	77

Figure

Page

- |    |  |    |
|----|--|----|
| 34 | Tare (No Flow) Shot for Comparison with Figure 33                                | 78 |
| 35 | Near-Field Phase Map from Interferogram Reduction;<br>Only Tilt has been Removed | 79 |

## 1.0 INTRODUCTION

This test report describes in detail the ABEL, single-pulse, preliminary beam quality measurements.

These measurements are explicitly labelled as preliminary in nature, for a variety of reasons. First, the funding and time made available for the task were strictly delineated. As a practical necessity, diagnostic development and data acquisition overlapped, and portions of the diagnostic configuration were left in an unperfected state, in order that a representative data base could be obtained. Further, the device was operated under reduced energy conditions; extrapolation to higher energies is speculative. Finally, and most significantly, the task guidelines stipulated that no effort was to be made to tune, adjust, or modify the laser to optimize beam quality; the experiments were strictly open-loop. Thus, these measurements cannot be said to define the beam quality obtainable from rep-pulsed CO<sub>2</sub> lasers in general or even ABEL, in particular, and should not be so construed.

Nevertheless, in spite of these constraints and caveats, the experiments were on the whole quite successful. The IR photography-based diagnostic proved to be at least as accurate as any previously used. With a little more work (for improved near-field energy measurement) it should prove vastly superior.

The measured beam quality for ABEL was quite reasonable, given the lack of opportunity for device adjustment. A large portion of the observed focal spot distortion was apparently caused by astigmatism, though its source remains unclear at this time. There is every reason to believe, that with this astigmatism corrected, the original beam quality specifications for ABEL are fully attainable.

### 1.1 EXPERIMENTAL OBJECTIVES

The objectives of this task were to:

- develop a reliable beam quality measurement technique;
- obtain data on ABEL on an "as-is" basis;
- evaluate medium quality interferometry as a beam quality predictive tool; and
- evaluate near-field-to-farfield energy delivery.

## 2.0 EXPERIMENTAL METHOD

### 2.1 CONCEPT OF DIAGNOSTIC

#### 2.1.1 Previous Techniques

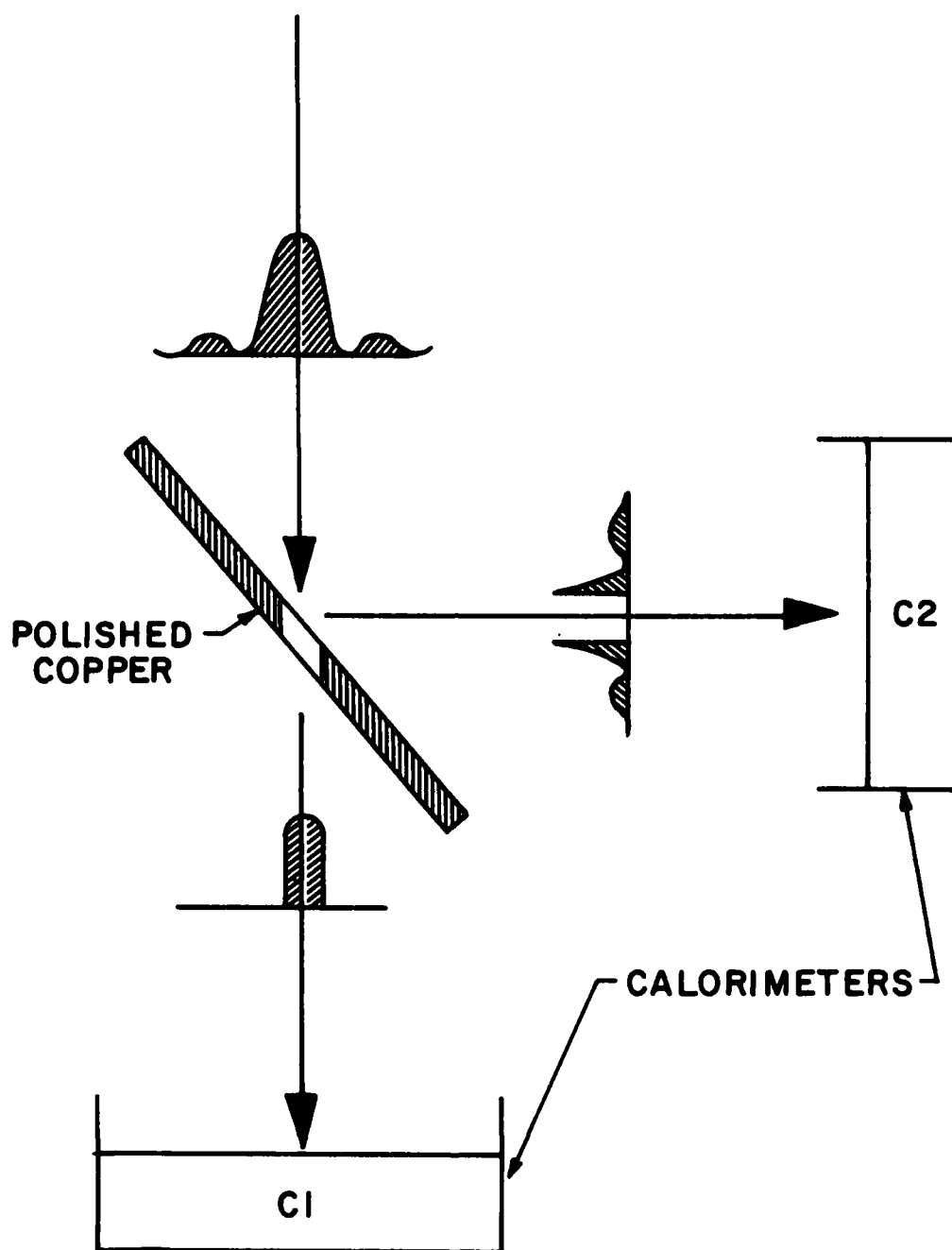
A common technique to make qualitative and semi-quantitative assessments of infrared laser beam properties is to make burn patterns on thermofax paper, projection transparency (vu-graph) plastic, or similar such material. These materials turn color and undergo surface damage at increasing energy density exposures, and thus provide an approximate photograph of the beam. Unfortunately, the response of the material is not linearly related to the IR exposure, and the overall dynamic range from threshold to disintegration is rather limited. Nonetheless, burn patterns are quick and easy and so remain useful for alignment, focal plane determination, and similar tasks.

For more quantitative work, so-called "power-in-the-bucket" methods (actually, energy in the bucket) have been used. In its simplest form, the farfield focal spot is sampled by an aperture plate as depicted in Figure 1, with the two calorimeter readings  $C_1$  and  $C_2$  used to compute a beam quality number.

There are two disadvantages to direct power-in-the-bucket measurements. Since the experimental data consist of just two numbers,  $C_1$  and  $C_2$ , no information about the details of the energy distribution are preserved. As will be apparent later in this report, such detailed information is very useful in identifying beam aberrations, as the common aberrations have distinctive effects on focal spots.<sup>(1)</sup> Further, the results of the measurement are highly sensitive to the alignment of the aperture plate on the farfield spot. Any component misalignment or beam jitter will degrade the computed value of beam quality to a degree which is difficult to determine after the fact.

More elaborate methods employing multiple aperture sampling have been devised<sup>(2)</sup> but again careful alignment is essential.

1. Born & Wolf, Principles of Optics, 5th ed. (Pergamon, London), Ch. 9.
2. O'Neil, R.W., Kleiman, H., Marquet, L., Kilcline, C., and Northam, D., Applied Optics 13, 2 (February 1974), pp. 314-321.



H2434

Figure 1. Basic "Power-in-the-Bucket" Scheme for Laser Beam Quality

### 2.1.2 Diagnostic Concept Used for ABEL Preliminary Beam Quality

Development of a practical IR photography scheme allows beam quality measurements which combine the best features of burn patterns and power-in-the-bucket measurements, while avoiding their drawbacks. The only disadvantage introduced by a photography-based system is the time delay required for film processing (~1/2 day) and for quantitative data analysis. For the ABEL experiments, with no programmatic provision for beam optimization, this was of no consequence and would have posed only a minor inconvenience were beam optimization carried out.

An overall beam quality measurement diagnostic design was formulated incorporating several separate physical measurements. These measurements were:

- 1) Near-field energy,  $E_{nf}$
- 2) Near-field time-dependent intensity,  $I_{nf}(t)$
- 3) Farfield energy,  $E_{ff}$
- 4) Farfield time-dependent intensity,  $I_{ff}(t)$
- 5) Farfield energy density (fluence) distribution,  $E_{ff}(x,y)$

In order to avoid sampling errors caused by local hot spots, it was originally intended that the near-field diagnostic use a polyethylene membrane beam splitter to achieve uniform sampling. Also, to avoid shot-to-shot variations, all quantities were to be measured on every shot. Practical difficulties forced us to relax these plans somewhat, in order to accumulate a useful amount of data by the scheduled end of the experiments. In particular, near-field energy was calculated from cavity input energy, and not measured on a shot-by-shot basis. The error introduced by doing this constituted the dominant source of uncertainty for the beam quality measurements. It appears, however, that with some further work it would be possible to make all measurements concurrently.

## 2.2 EXPERIMENTAL SETUP

### 2.2.1 General

The room layout of the major components, except for the near-field diagnostic, is shown in Figure 2. The beam travels 5.8 m through an attenuating screen to a focus mirror ( $f = 68$  m), then 19 m to a folding flat, 19 m through a second screen to another folding flat, 14.2 m to a salt wedge beam splitter, and finally



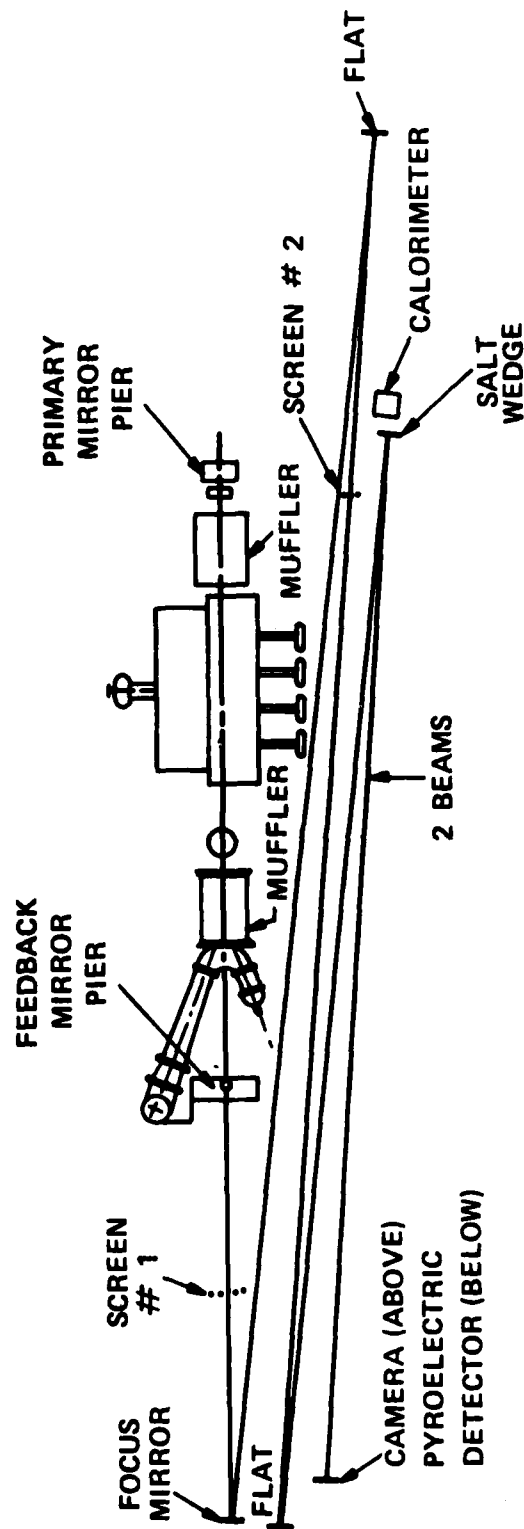


Figure 2. Room Layout for ABEL Preliminary Beam Quality Measurements

back 14.3 m to the focal plane. The actual focal distance was determined experimentally as 66.5 m; evidently the beam from the cavity was very slightly converging. Observed depth of field was  $\sim \pm 1$  m.

The choice of focal length was determined by two factors. First, it was desirable to have a reasonably sized farfield spot. A larger focal spot minimizes the overall system attenuation required. Second, the diffraction order spreading angle of the attenuator screens dictated a certain minimum path length to ensure order separation. The distances selected allowed the side orders from screen #1 to separate at the first flat, where they were blocked; the orders from the second screen were separated at the salt wedge beam splitter.

The folded optical path was confined as compactly as possible, with all the beams fitting into a 7 ft high (for headroom) by 7 ft wide cross-section duct. The purpose of this duct was to minimize the effects of room temperature gradients and air turbulence, and to prevent any leaking laser gas from squirting into the optical path.

Another constraint on the location of optical paths was to minimize the astigmatism induced by striking the focus mirror at non-normal incidence. Astigmatism is generally the dominant aberration in such beam trains. The extra XDL multiplier resulting from this astigmatism is approximately\*

$$\text{XDL (astigmatism)} \cong 1 + 0.01 \left[ \frac{D^2}{f\lambda} \theta^2 \right]^2 \quad (1)$$

where  $2\theta$  = angle between incoming and outgoing beams. For the ABEL experiments,  $2\theta = 7.5^\circ$ . Then

$$\text{XDL (astigmatism)} = 1.003,$$

which is negligible.

### 2.2.2 Attenuator Screens

The beam path attenuator screens were thin electro-deposited sheets of copper or nickel, with the holes arranged as a hexagonal array. Only the zero order was used. Extra attenuation was achieved by cascading screens, with the second screen placed in

\*Smith, M.J., AERL Memorandum, 16 September 1977. This formula only holds for small amounts of astigmatism. Also, this astigmatism is unrelated to any arising in the cavity.

the farfield of the first. Then the net attenuation was just the product of the two farfield attenuations. This was verified by measurement. Table 1 summarizes the relevant properties of the screens.

TABLE 1. ATTENUATOR SCREENS FOR ABEL PRELIMINARY BEAM QUALITY

	<u>Screen A</u>	<u>Screen B</u>	<u>Screen C</u>
Material	Copper	Copper	Nickel
Hole Diameter	0.125 cm	0.063 cm	0.040 cm
Nominal Open Area	50%	22%	14%
Measured Farfield Transmission	$0.230 \pm 0.005$	$0.042 \pm 0.001$	$0.024 \pm 0.001$
Order Separation Angle	0.00625	0.0083	0.010

Attenuator #1 (Figure 2) was subjected to the direct near-field fluence of ABEL, which for these experiments ranged up to  $12 \text{ J/cm}^2$  average. Experience has shown that screens, when used in an "as received" condition will suffer surface plasma detonations (disrupting their transmission grating properties) for fluences greater than about  $5 \text{ J/cm}^2$ . To avoid this problem, screens used for the first attenuator were ground and polished like mirrors, and mounted for use in a tunnel enclosure swept at all times by "class 100" filtered air.\* Previous experiments on the Humdinger Laser has shown that polished screens, so enclosed, would readily withstand at least  $12 \text{ J/cm}^2$ . We carefully monitored the screen surfaces during the ABEL test runs, and did not observe any plasma flashing on the screen surface or within the holes.

### 2.2.3 Farfield Diagnostic

Figure 3 further details the farfield portion of the beam quality optical train. The ABEL beam, converging toward focus, strikes a salt wedge mounted directly in front of a small ( $3\text{-}1/2$ " useful aperture) flat plate calorimeter. The front surface reflection was directed toward the IR camera; the rear surface

\*Ray Products Co. (El Monte, CA) Model RPC-00-15B blower-filter system. Class 100 means  $<100$  particles/ $\text{ft}^3$  of size  $\geq 0.5 \mu\text{m}$ ; this is considered very clean air.

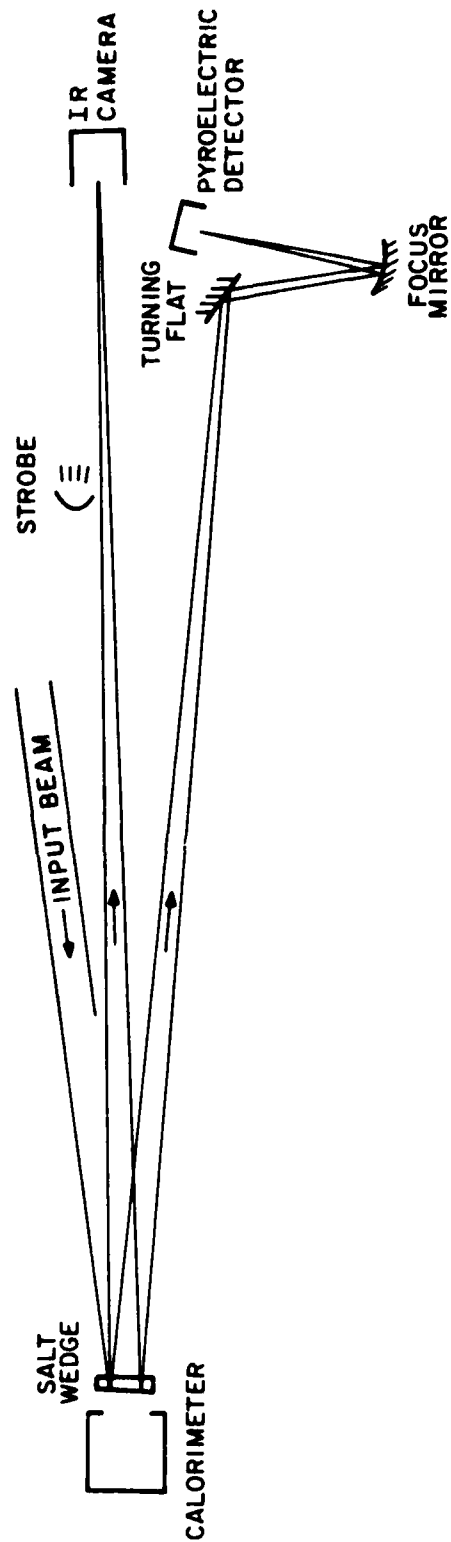


Figure 3. Farfield Schematic

J8553

reflection was aimed at the farfield I(t) detector. The angle between the two reflected beams was about 4.5°. The salt wedge was oriented to provide over-and-under rather than side-by-side reflections, in order to keep within the confines of the beam ducting discussed earlier.

The focal spot from the rear-surface salt wedge reflection did not directly strike the I(t) pyroelectric detector, but rather was re-imaged by a demagnifying mirror. This was an attempt to reduce the I(t) detector alignment sensitivity to tolerable levels. This arrangement was not completely satisfactory, and, as a result, we took farfield I(t) data for only a few shots. For future measurements, it is clear that a collecting cone would be a useful addition.

Since the reflectivity of salt is 0.039 (measured) at 10.6  $\mu\text{m}$ , the salt wedge and calorimeter obviously must survive fluences  $\sim 25$  times higher than that reflected towards the IR camera and pyroelectric detector. This limits how close to the system focus the salt wedge and farfield calorimeter can be placed.

One can estimate the minimum distance as follows. Suppose a uniform nearfield fluence  $E_{\text{NF}}$  (Figure 4) is perfectly focussed to a spot of peak fluence  $E_{\text{ff}}$  after being attenuated by a factor  $\alpha$ . The well-known diffraction relationship between  $E_{\text{nf}}$  and  $E_{\text{ff}}$  is

$$\frac{E_{\text{ff}}}{E_{\text{nf}}} = \left( \frac{A}{\lambda f} \right)^2 \alpha \quad (2)$$

where A is the area of the near field. We estimate geometrically the average fluence  $E_z$  at a distance z, assumed larger than the depth of focus, as

$$E_z = \alpha E_{\text{nf}} \left( \frac{f}{z} \right)^2 \quad (3)$$

or

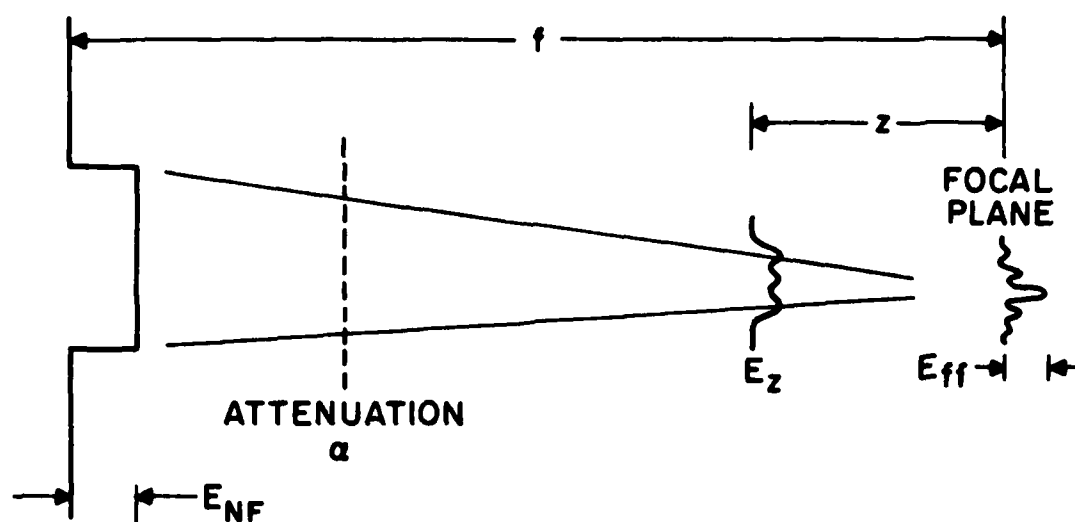
$$E_z = E_{\text{ff}} \left( \frac{\lambda f^2}{Az} \right)^2$$

from which

$$z = \left( \frac{E_{\text{ff}}}{E_z} \right)^{1/2} \frac{\lambda f^2}{A} \quad (4)$$

For  $E_{\text{ff}} = 1.5 \text{ J/cm}^2$ ,  $E_z = 0.25 \text{ J/cm}^2$ ,  $f = 6650 \text{ cm}$ , and  $A = 240 \text{ cm}^2$ , we have

$$z_{\text{min}} \sim 5 \text{ m}$$



J9250

Figure 4. Geometry for Estimating Salt Beamsplitter Placement

To permit cavity access, it turned out to be convenient to locate the salt wedge and farfield calorimeter about 13 m from the focal plane.

#### 2.2.4 I(t) Detectors

The shielding arrangement used to ensure clean signals on the pyroelectric detectors used for I(t) measurements is shown in Figure 5. The detectors were mounted coaxially inside nested iron pipes for magnetic shielding. The outer iron pipe was wrapped with copper screen, which was connected via braid shielding to the outside of the instrumentation screen room. The detectors themselves were connected by semi-rigid coaxial cable to oscilloscopes. The coaxial cable ground and the braid shielding ground were carefully kept insulated from each other and from all grounds in the device room.

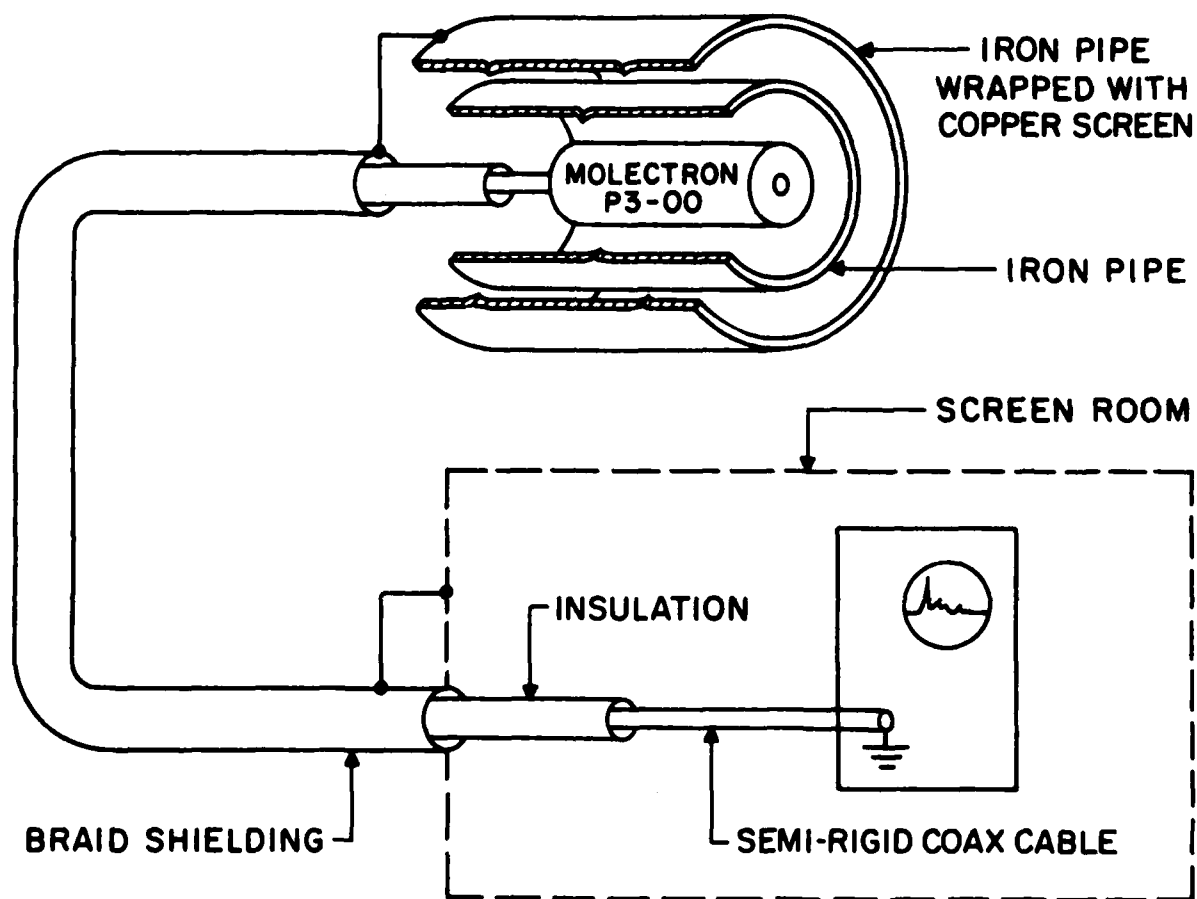
Molelectron type P3-00 pyroelectric detectors were used for both near and farfield I(t) measurements. These detectors incorporate built-in amplifiers which match to 50  $\Omega$  cable. The frequency response is determined by a load resistor; for these measurements, a  $10^3 \Omega$  resistor was used, providing a 3 dB rolloff at about 75 MHz. Responsivity was about  $2 \times 10^{-4}$  V/W.

#### 2.2.5 Near-Field Diagnostic

Figure 6 shows the final version, near-field diagnostic layout used for the I(t) measurements. The source of photons was non-specular reflection from the #1 attenuator screen. These were intercepted by a pickoff mirror, and collected onto the pyroelectric detector by a polyethylene Fresnel lens.

Because the detector looks at the screen (at a fairly short object distance) and not the beam itself (which is effectively a source at infinity) this arrangement provides in fact, a whole-beam sample. The direct specular reflection of the beam went around the pickoff mirror to a beam dump.

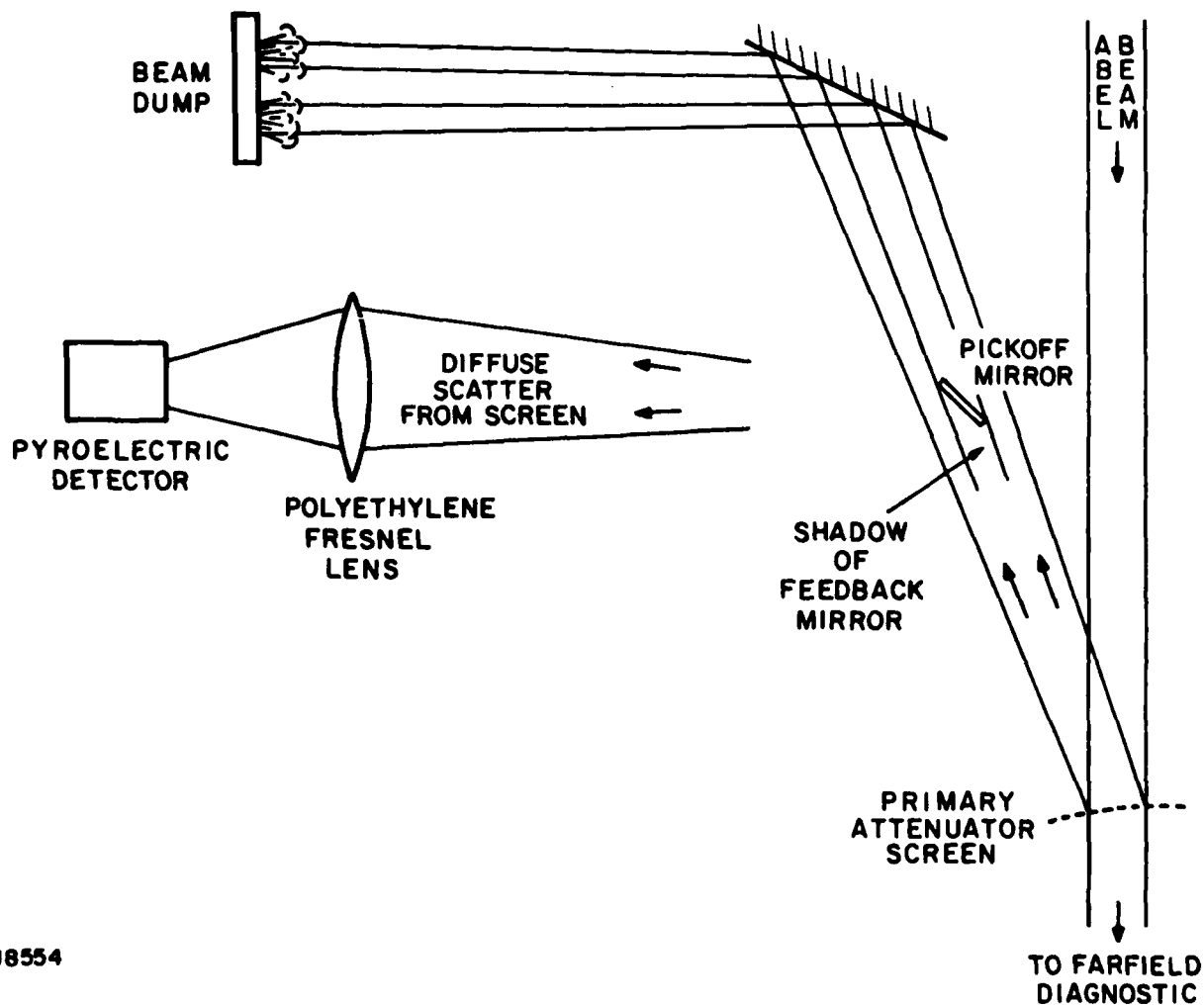
The key feature of this diagnostic is the capture of the energy reflected by the screen. We initially attempted to utilize the direct specular reflection, in principle a better method. Unfortunately, residual wrinkles and dimples in the polished grating caused catastrophic flux concentrations on the collection optics, leading to plasma breakdowns which made the  $I_{nf}$  and  $E_{nf}$  readings unreliable. We tried to overcome this difficulty by mounting the screen in a tension frame which stretched the screen in the vertical direction while bowing it slightly in the horizontal. This frame helped considerably - the arrangement of Figure 6 wouldn't have worked with an unstretched screen - but there were



J8431

Figure 5. Shielding Arrangement for Molelectron Pyroelectric Detectors





J8554

Figure 6. Near-Field Schematic

still a number of (less severe) hot spots. A promising improved frame with "two-way stretch" was started but not finished by the end of the experiment period.

The degree of screen wrinkling after polishing was observed to depend, to a considerable degree, on the mechanical properties and handling history of the stock material. We ended up using the nickel screen (screen C in Section 2.2.2) for attenuator #1 because it was stiffer and apparently had been handled less. Since these screens are generally used for sieves, the manufacturer does not take any special precautions for handling or storage, and their long lead time precluded our using any but stock screens

#### 2.2.6 Near-Field Energy

These difficulties also prevented us from incorporating a meaningful shot-by-shot energy measurement into the near-field diagnostic. As an alternative, near-field energy for each shot was indirectly computed as follows. At several times during the test period, full-beam calorimeter shots were taken. For these shots, the first attenuator screen was temporarily removed, and an expanding mirror placed in the beam path just in front of the focus mirror. The magnified near-field image was then directed onto a large ribbon calorimeter. The ribbon calorimeter was sufficiently large to ensure capture of any large-angle energy.

Current and voltage traces for each test shot were digitized and used as inputs to AERL's CO<sub>2</sub> kinetics code, yielding predicted ABEL output energies. Computer results for calorimeter shots were compared with the measured output for those shots to give efficiency calibration factors. For those data shots taken on a day during which a calorimeter shot was also taken, the calibration factor from that day's calorimeter shot (only) was used to assign near-field energies to the data shots. For those data shots taken on a day during which no calorimeter shot was taken, the average calibration factor from all calorimeter shots was used. The scatter in calibration factors was  $\pm 15\%$ ; we have applied this uncertainty as the error to be associated with the data shot near field energy values.

The near-field energy uncertainty is larger than that of any other parameter of the experiment, and defines the error associated with those results depending on it. In particular, the farfield/near-field energy ratio and one of two beam quality (XDL) calculation methods are affected. Nevertheless, even a  $\pm 15\%$  uncertainty is quite good for high energy measurements of this sort.

### 2.3 10.6 $\mu\text{m}$ PHOTOGRAPHY

Ordinarily, photographic films do not respond to 10.6  $\mu\text{m}$  radiation except by undergoing burn damage. While this is useful for location and approximate characterization of laser beams, it clearly is not sufficient for quantitative analysis.

AERL has developed a technique whereby pulsed infrared sources may be photographed, based on the varying exposure sensitivity of certain films to transient heating. For more complete details, the reader is directed to Reference 3, but a brief description follows. Figure 7 illustrates the process. An infrared pulse strikes the film and is absorbed, converting the beam's spatial fluence distribution into a temperature distribution within the film. Then, before the heat can diffuse, a narrow-band visible pulse exposes the film capturing an image of the laser beam. The wavelength of the visible pulse, its intensity, and the type of film, must be carefully chosen to maximize the dynamic range and the IR sensitivity of the process.

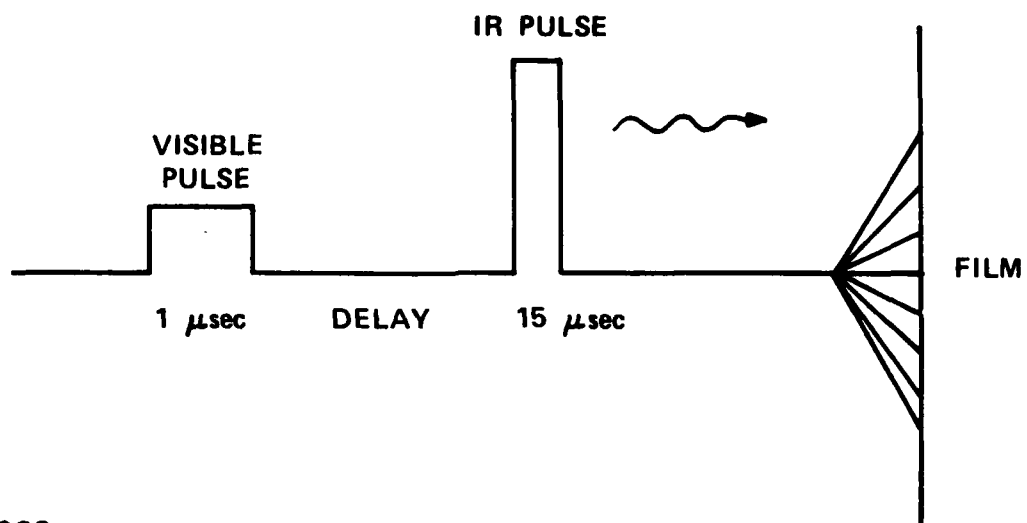
Figure 8 shows the response curve appropriate for 15  $\mu\text{s}$  ABEL pulses (the response depends slightly on IR pulse length and goes up approximately 30% if pulse length is reduced by a factor of 100). The calibration is accurate to better than 2% in image density and better than 4% fluence, for fluences up to about 1.25 J/cm<sup>2</sup>. At higher fluences, the film begins to physically degrade, exhibiting an erratic response, with the emulsion detaching from the film base. At  $\geq 1.7$  J/cm<sup>2</sup> the emulsion is destroyed. Figure 8 was used to analyze the ABEL farfield pictures. To minimize error, we used the same calorimeter for film calibration as was used for ABEL farfield energy.

Beam quality may be determined directly from focal spot pictures, either by reading the central spot peak intensity, or by integrating the energy within an arbitrary bucket. For example, Figure 9 shows the focal spot of a 64 cm<sup>2</sup> circular sample from the near-field of Avco's Humdinger laser. Applying the second method to the iso-intensity contour map of the picture, a straightforward calculation gives a beam quality of 1.07 XDL. Specific calculations for ABEL are given in Section 4.4 below.

### 2.4 INTERFEROMETRY SETUP

To provide a basis of comparison for the beam quality results, interferograms were taken for the same conditions as the data runs. This will be discussed further in Sections 3.0 and 4.5.

3. Naor, D., Flusberg, A., and Itzkan, I., "Infrared Laser Photography with Silver Halide Emulsion," to be published in Applied Optics (August 1981).



J7089

Figure 7. Infrared Photography with Silver Halide Film

## IR FILM RESPONSE

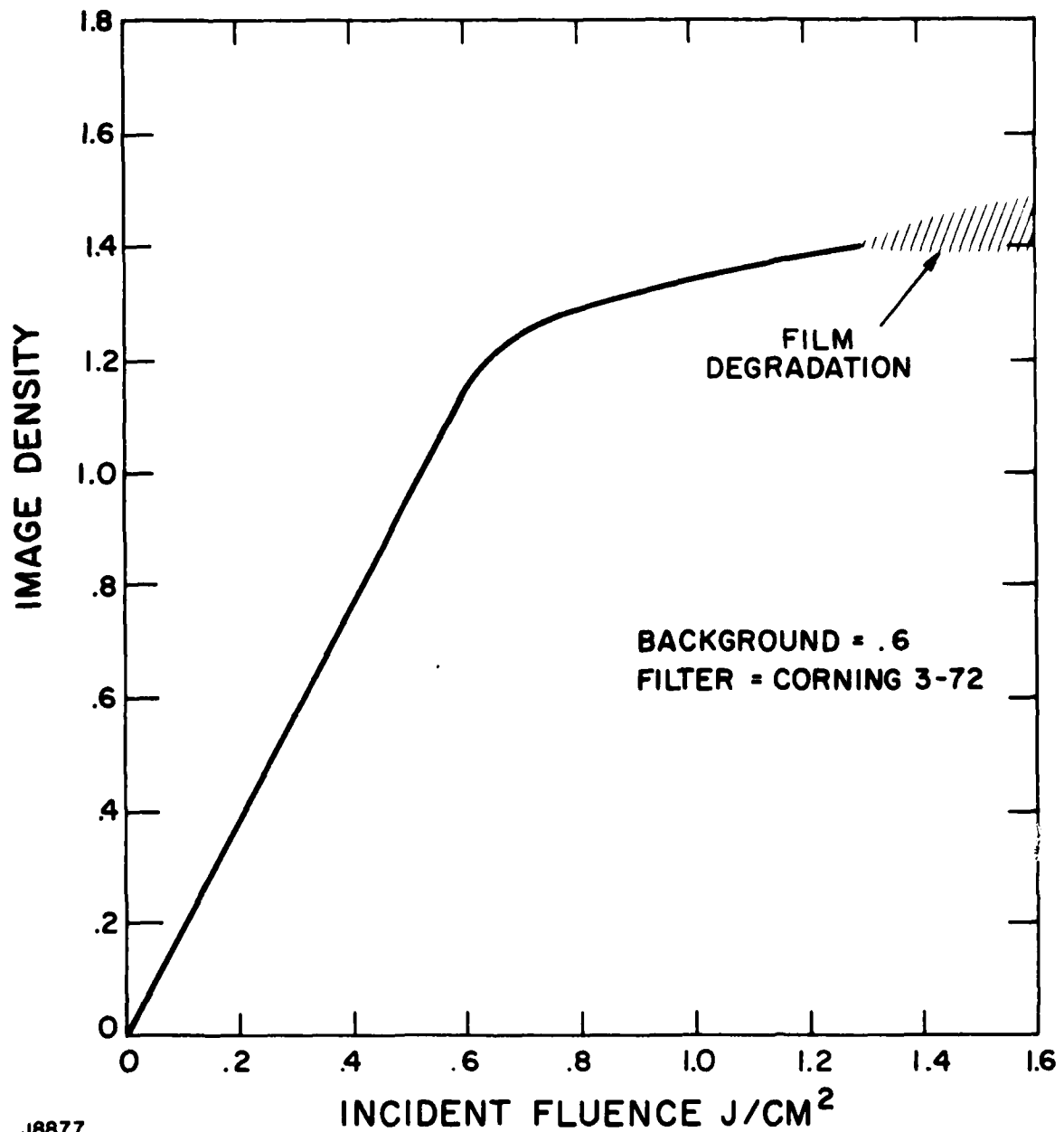


Figure 8. Infrared Film Calibration Curve for ABEL Measurements

# MEASURED BEAM QUALITY : 1.07 XDL

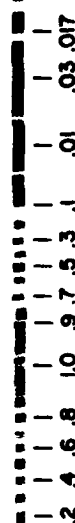
POSITIVE PRINT

(PRINT HAS BEEN OVEREXPOSED TO SHOW WEAK RING)

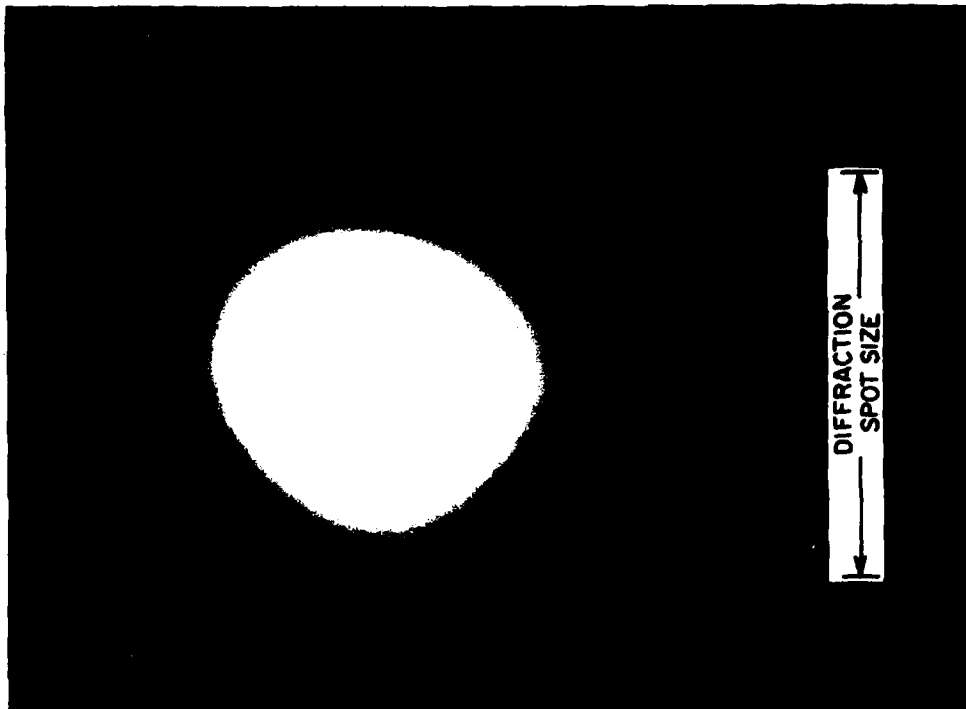
INTENSITY CONTOUR MAP



RELATIVE INTENSITY



J8997

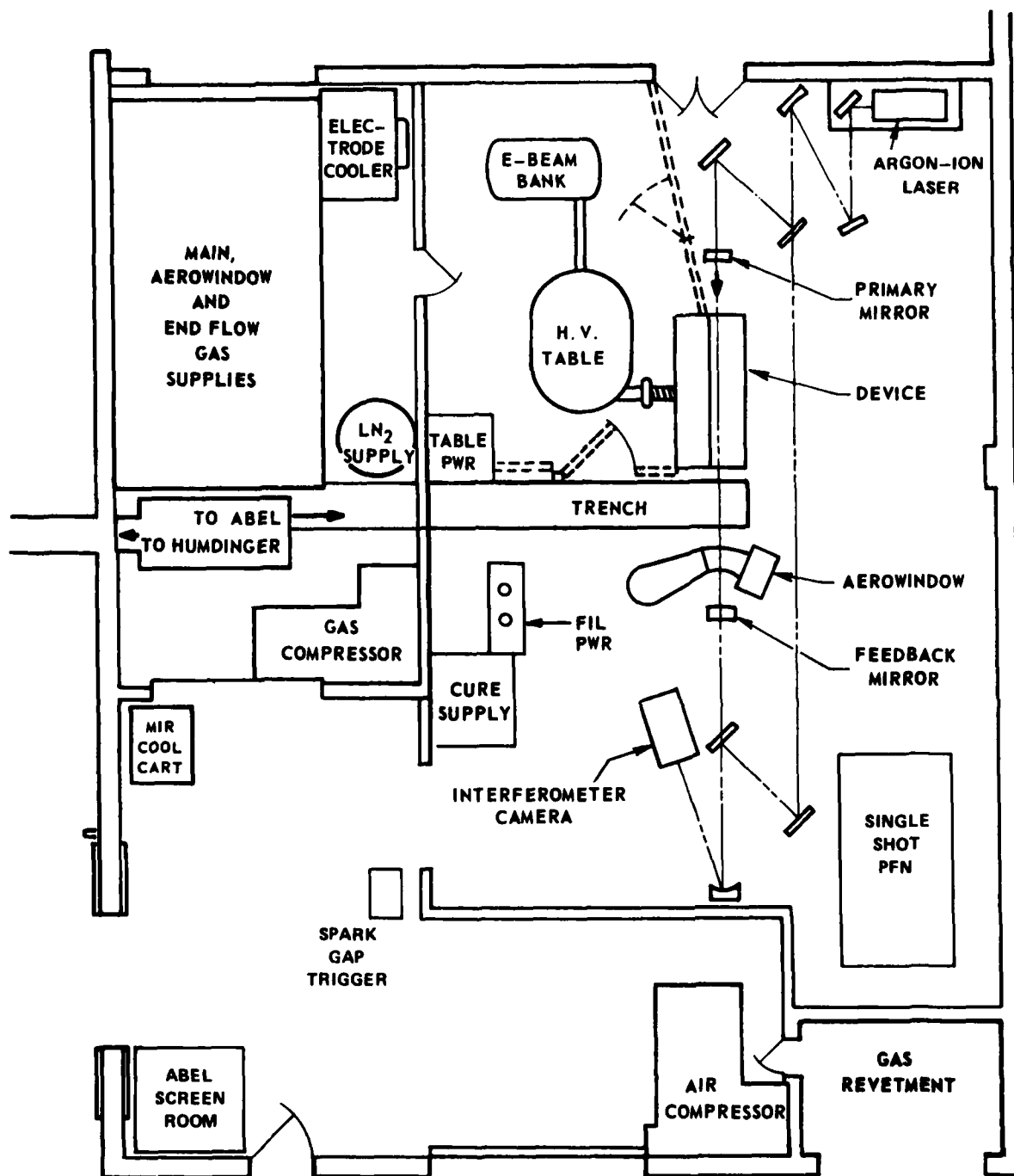


(HUMDINGER LASER, OCT. 1980)

Figure 9. Focal Spot Infrared Photograph of CO<sub>2</sub> Pulsed Electric Discharge Laser Far Field Beam

The interferometer used was of the Mach-Zehnder configuration employed in previous ABEL diagnostic work (Figure 10). The beam splitter optics for this interferometer were smaller than the 27 cm mode height of ABEL. As a result, the field of view of the interferometer was chosen, as in the past, to cover only the downstream 2/3 of the gas flow, which is physically the top 2/3 of the resonator mode area.

Laser illumination was provided by a 0.514  $\mu\text{m}$  cw argon-ion device, with a high-speed movie camera recording the results. A pulsed xenon laser for planned short exposure (much less than ABEL pulse length) work failed and could not be repaired within the test period.



61692

Figure 10. Interferometry Diagnostic for ABEL



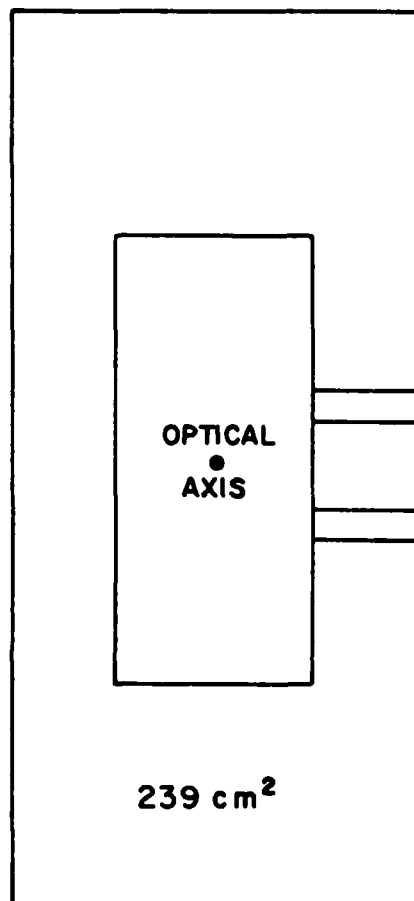
### 3.0 TEST DESCRIPTION

Though beam quality optimization was outside the scope of these experiments, a certain degree of systematic operating parameter variation was included in the test plan, to see if any change was evident in the laser optical performance. Parameters varied were gas flow rate (from 2.5 to 4.2 cm/ms), output energy (2.0 to 2.8 kJ), and resonator configuration (centered and off-center optical axis). Not all combinations were tried, and not all of the elements of the diagnostic were always operating for those combinations that were tried. Farfield energy measurements and IR photos were taken for all the data points, whereas  $I(t)$  traces were taken for only a very few, because of the time consuming nature of the farfield  $I(t)$  alignment.

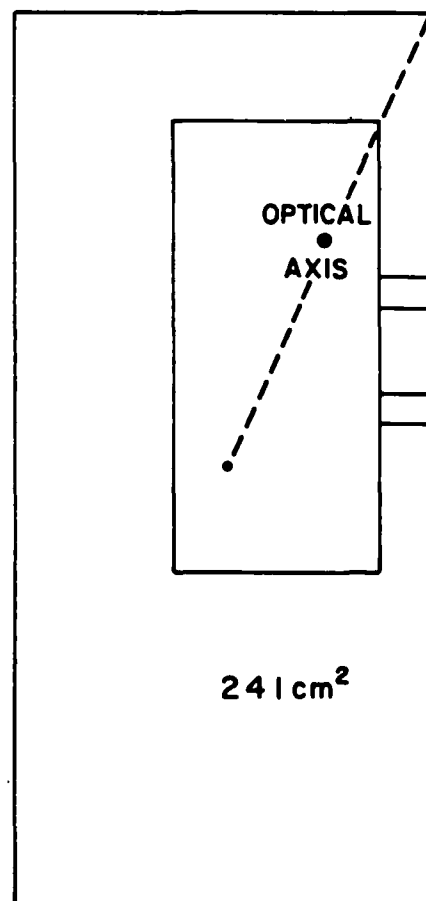
In all cases, a 3:1:0.08 ( $N_2:CO_2:H_2$ ) gas mixture was used, with gas temperature approximately 270°K. Geometric output coupling was 75%.

The two resonator configurations are depicted in Figure 11. The view is from behind the feedback mirror looking into the cavity. For the off-center case, the feedback mirror was moved so that the optical axis was situated along a diagonal, halfway to the corner. Because less of the support was visible for the off-center mounting, the near-field area increased slightly in that case.

Cavity interferograms were taken with core flow only, core flow plus end flow, and full system flow, at both low and high mass flow rates.



CENTERED  
OBSCURATION



OFF-CENTER  
OBSCURATION

MODE SIZE  
=  $12 \times 27 \text{ cm}^2$   
=  $324 \text{ cm}^2$

J9253

Figure 11. Resonator Configuration Used for Beam Quality Tests

## 4.0 TEST DATA

### 4.1 FARFIELD/NEAR-FIELD ENERGY COMPARISON

#### 4.1.1 Experimental Issue

An important issue for HEL applications is energy delivery to the farfield. It has in the past often been implicitly assumed that the total optical energy output measured near the laser can be focused to the farfield, with imperfections and distortions in the focal spot describable by a "times diffraction limited" number.

It has more recently become apparent that the true situation is more complicated. Specifically, a certain fraction of the near-field energy does not focus to the region of the farfield diffraction pattern. The net result is an apparent attenuation of the useful beam. One of the objectives of these experiments is to measure the extent of this energy loss for ABEL, looking for any variation with laser operating conditions. We also want to see to what degree it can be predicted by cavity interferometry (this latter is discussed separately in Section 4.5).

It must be noted that beam quality measurements using only a power-in-the-bucket scheme in the farfield will not detect this energy loss, and that any times-diffraction-limited number so derived will by itself render an incomplete description of a laser's optical performance. For that reason, and also because different causal mechanisms may be at work, we adopt the convention in this report of characterizing optical performance by two quantities: a farfield/near-field energy ratio,  $\eta$ , (representing an energy-delivery efficiency) and a beam quality XDL or times-diffraction-limited number characterizing energy distribution in the immediate vicinity of the focal spot.

#### 4.1.2 Test Data

A total of 24 data shots were taken. The results of these are depicted on Figure 12, where the farfield/near-field ratio is plotted as a function of near-field energy. Three different operating conditions are shown: centered resonator with low flow, centered resonator with high flow, and off-center resonator with low flow. Since the experimental uncertainty in near-field energy is coupled to that of the ordinate  $\eta$ , and is larger than that for the farfield energy, the error for each data point forms a long slanted parallelogram-shaped region as shown on the figure.

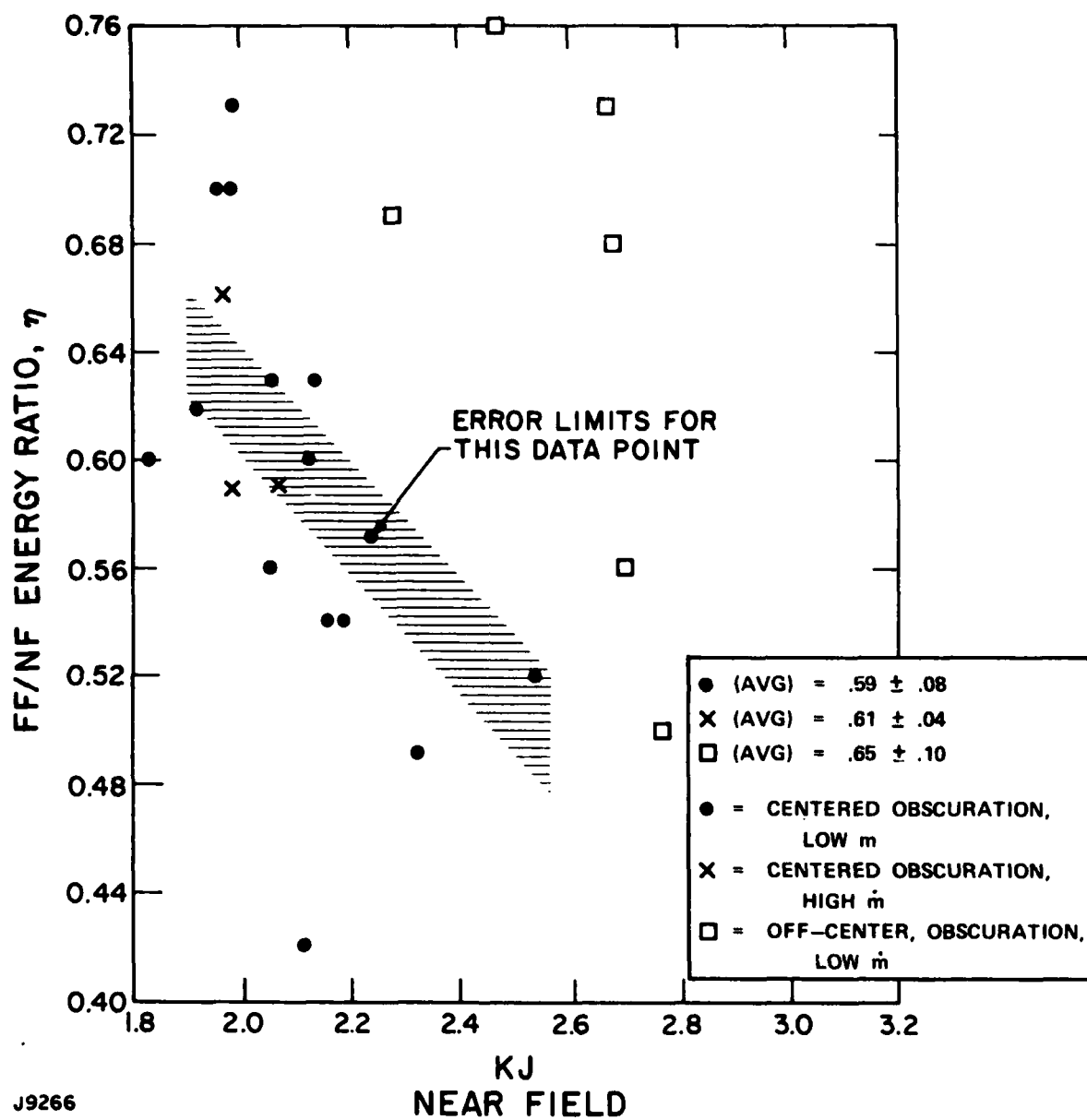


Figure 12. Farfield Energy Delivery Ratio vs Near-Field Energy. The shaded zone shows the extent of the uncertainty limits to be associated with the data.

It had been hypothesized that increasing the laser energy might improve the energy transfer ratio, because of the increasing saturation of the gain medium. A regression analysis of all the data points on Figure 12 gives a correlation coefficient of -0.026; i.e.,  $\eta$  is essentially uncorrelated with laser energy, at least in the 2.0 to 2.8 kJ range. The other variables (mass flow and resonator configuration) also appear not to affect  $\eta$ , though one might argue that the slight improvement for the off-center resonator case is real and not statistical.

To summarize, then, the energy transfer ratio was found to be essentially constant for these experiments, with a value of 60-65%.

#### 4.1.3 Possible Explanations

A number of explanations have been put forward to explain the energy loss, and we review and comment on them here.

##### Calorimeter Error

Since the near-field and farfield calorimeters were designed to respond to energy levels differing by three orders of magnitude, there is no easy way to calibrate both simultaneously. Calibration of the near-field ribbon calorimeter is discussed in the Low Average Power Test Report. The farfield calorimeter was calibrated by direct comparison with other small previously characterized calorimeters, using a known beam splitter to send beams to both the reference and test calorimeters.

We believe that both the near and farfield calorimeters are accurately calibrated. But, since they were calibrated separately, there remains a slight possibility that one or the other of the calibrations was in error, accounting for the observed values of  $\eta$ .

##### Amplitude Grating

Harvey<sup>(4)</sup> has proposed that diffraction ripples present in the near field of an HEL beam act as an amplitude grating, similar to the attenuator screens. By examining near-field burn patterns in plastic, he models the amplitude as

$$U(x,y) = U_1(x)U_2(y) \quad (5)$$

4. Harvey, J.E., et al., University of Dayton Research Institute Technical Report, UDRI-A-193 (May 1980; Revised June 1980).

where

$$U_1(x) = [1 + A \cos(2\pi\alpha_1x)] + [1 + C \cos(2\pi\alpha_2x)] \quad (6)$$

$$U_2(y) = [1 + B \cos(2\pi\beta_1y)] + [1 + E \cos(2\pi\beta_2y)]$$

with A, B, C, D,  $\alpha_1$ ,  $\alpha_2$ ,  $\beta_1$ , and  $\beta_2$  adjusted to mimic the structure seen in the intensity pattern

$$I(x,y) = |U(x,y)|^2 \quad (7)$$

The transmitted energy fraction in the central order of this grating is given by

$$\eta(\text{grating}) = \left\{ 1 + 2 \left( \frac{A}{4} \right)^2 + 2 \left( \frac{B}{4} \right)^2 + 2 \left( \frac{C}{4} \right)^2 + 4 \left( \frac{AB}{16} \right)^2 + 4 \left( \frac{CB}{16} \right)^2 + 4 \left( \frac{AD}{16} \right)^2 + 4 \left( \frac{CD}{16} \right)^2 \right\}^{-1} \quad (8)$$

In order to get a value for  $\eta(\text{grating})$  that agrees with experiment, the model must have A, B, C, and D all at or very close to unity. This in turn implies zeroes or near-zeroes in the intensity pattern.

A careful examination of the near-field intensity distributions of a variety of rep-pulsed CO<sub>2</sub> lasers (not just ABEL) fails to show any such degree of modulation. Figure 13 shows a typical portion from an IR photograph scan of a near-field sample; peak intensity variations about the mean are no more than 30%. In the model defined by Eqs. (5) through (8) we hold  $U_2(y) = \text{constant}$  (since we have a one-dimensional scan) and let  $C = A$  for simplicity. Then the resulting nominal variation of I is

$$\frac{I_{\text{max, min}}}{I} = \frac{1}{4} |U_1|^2_{\text{max, min}} \implies 1 \pm 2A \quad (9)$$

so that  $A = 0.15$ . The same degree of modulation is found along the other axis; using  $A = B = C = D = 0.15$  in Eq. (8) gives

$$\eta(\text{grating}) = 0.988$$

If we allow the peak intensity excursions to be  $\pm 75\%$ , considerably in excess of what has been measured,  $\eta(\text{grating})$  is still greater than 93%.

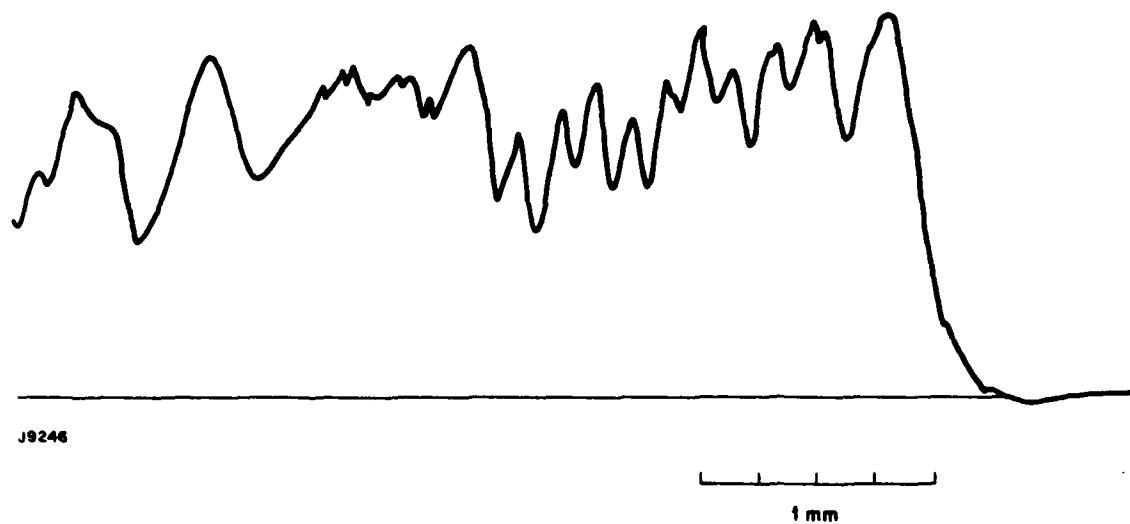


Figure 13. Typical Intensity Profile of Pulsed CO<sub>2</sub> Laser Beam

We conclude that this model, used with realistic coefficients, cannot explain the observed energy transfer ratio.

### Absorption

Another suggestion is that laser gas leaking from the cavity accumulates to an extent sufficient to absorb an appreciable fraction of the beam.

To estimate what amount of CO<sub>2</sub> would be needed to cause significant absorption, we use (after P. Ulrich, MIT Lincoln Lab) the single-pulse transient blooming formula

$$\frac{I}{I_0} = 1 - \delta \frac{3N}{2\pi} (\gamma - 1) \alpha E t^2 k^4 \left(\frac{a}{k}\right)^2 \quad (10)$$

where

$\delta$  = a constant  $\approx 0.4$

$N$  = molecular refractivity = 0.154 cm<sup>3</sup>/gm for air

$\gamma$  =  $C_p/C_v$  = 7/5 for air

$\alpha$  = absorption coefficient

$E$  = energy delivered to focal point

$t$  = pulselength

$k$  = wave number

$a$  = radius of (assumed circular Gaussian) beam

$f$  = focal length

Solving for  $\alpha$ :

$$\alpha = \left(1 - \frac{I}{I_0}\right) \left[ \delta \frac{3N}{2\pi} (\gamma - 1) E t^2 k^4 \left(\frac{a}{f}\right)^2 \right]^{-1} \quad (11)$$

If we take  $a^2$  as the near-field beam area (240 cm<sup>2</sup>) and as a conservative estimate take  $E$  as the unattenuated laser energy (2500 J) then to obtain  $I/I_0 = 0.6$ , we require  $\alpha = 0.005/\text{cm}$ . Since the normal atmospheric absorptivity for CO<sub>2</sub> is  $6 \times 10^{-7}/\text{cm}$ , based on a normal fractional concentration of 0.03%, a concentration of



$$\left(\frac{5 \times 10^{-3}}{6 \times 10^{-7}}\right) \cdot (3 \times 10^{-4}) \approx 200\% \text{ CO}_2$$

would be needed in the ABEL device room to achieve the necessary absorptivity.

Clearly this is not the case. As a check, we obtained a commercial CO<sub>2</sub> measuring kit, and took readings in the Humdinger laser room after several hours of running. (ABEL had been disassembled by then in preparation for the subscale experiments.) No CO<sub>2</sub> was measured within the range of the instrument ( $\lesssim 0.1\%$  CO<sub>2</sub>) anywhere in the room. Inserting the instrument into the Humdinger aerowindow did give a reading, indicating that the CO<sub>2</sub> instrument was functioning.

Room absorption then may be dismissed as an explanation for the observed energy transfer ratio.

#### Small-Scale Turbulence Scattering

A more promising approach is to examine the ramifications of the scale size of the turbulence in the flowing laser medium. Assume a wavefront emerging from ABEL with a random RMS phase variation,  $\sigma$ , and correlation scale size,  $a$ , both Gaussian distributed. (We ignore here ordered phase aberrations.)

Then the resulting beam can be decomposed into two parts, (5) a specular beam and a scattered beam (pancake). The specular beam will be focused by the beam train optics to an Airy pattern at the focal point. The intensity of the Airy pattern is reduced by the factor  $e^{-(2\pi\sigma/\lambda)^2}$ .

Therefore, the energy in the pancake (normalized) is  $1 - e^{-(2\pi\sigma/\lambda)^2}$ .

The pancake spreads at an angle of  $\lambda/\pi a$ . For  $a \ll D$  this is independent of the focusing optics. If a calorimeter intercepts a solid angle  $\Omega$  then it will collect  $\lambda^2/\Omega\pi^2 a^2$  of the pancake if  $\Omega < (\lambda/\pi a)^2$  and it will collect all of the pancake if  $\Omega > (\lambda/\pi a)^2$ .

5. Hogge, C., Butts, R., Burlakoff, M., Applied Optics, 13, 5 (May 1974), pp. 1065-1070.

A suitable function which approximates the above condition is  $1 - e^{-\Omega \pi^2 a^2 / \lambda}$ .

If  $\Omega_N$  is the solid angle subtended by the near-field calorimeter, and  $\Omega_F$  is the solid angle subtended by the farfield calorimeter, then the farfield signal is just

$$e^{-(4\pi\sigma/\lambda)^2} + \left[1 - e^{-(4\pi\sigma/\lambda)^2}\right] \left[1 - e^{-\Omega_F \pi^2 a^2 / \lambda^2}\right] \quad (12)$$

and the near-field signal

$$e^{-(4\pi\sigma/\lambda)^2} + \left[1 - e^{-(4\pi\sigma/\lambda)^2}\right] \left[1 - e^{-\Omega_N \pi^2 a^2 / \lambda^2}\right] \quad (13)$$

with the ratio of these quantities giving the energy transfer ratio  $\eta$ . For the geometry of these experiments,  $\Omega_F \approx (3\text{-}1/2 \text{ in.}/60 \text{ m})^2$  and  $\Omega_N = (1 \text{ m}/10 \text{ m})^2$ .

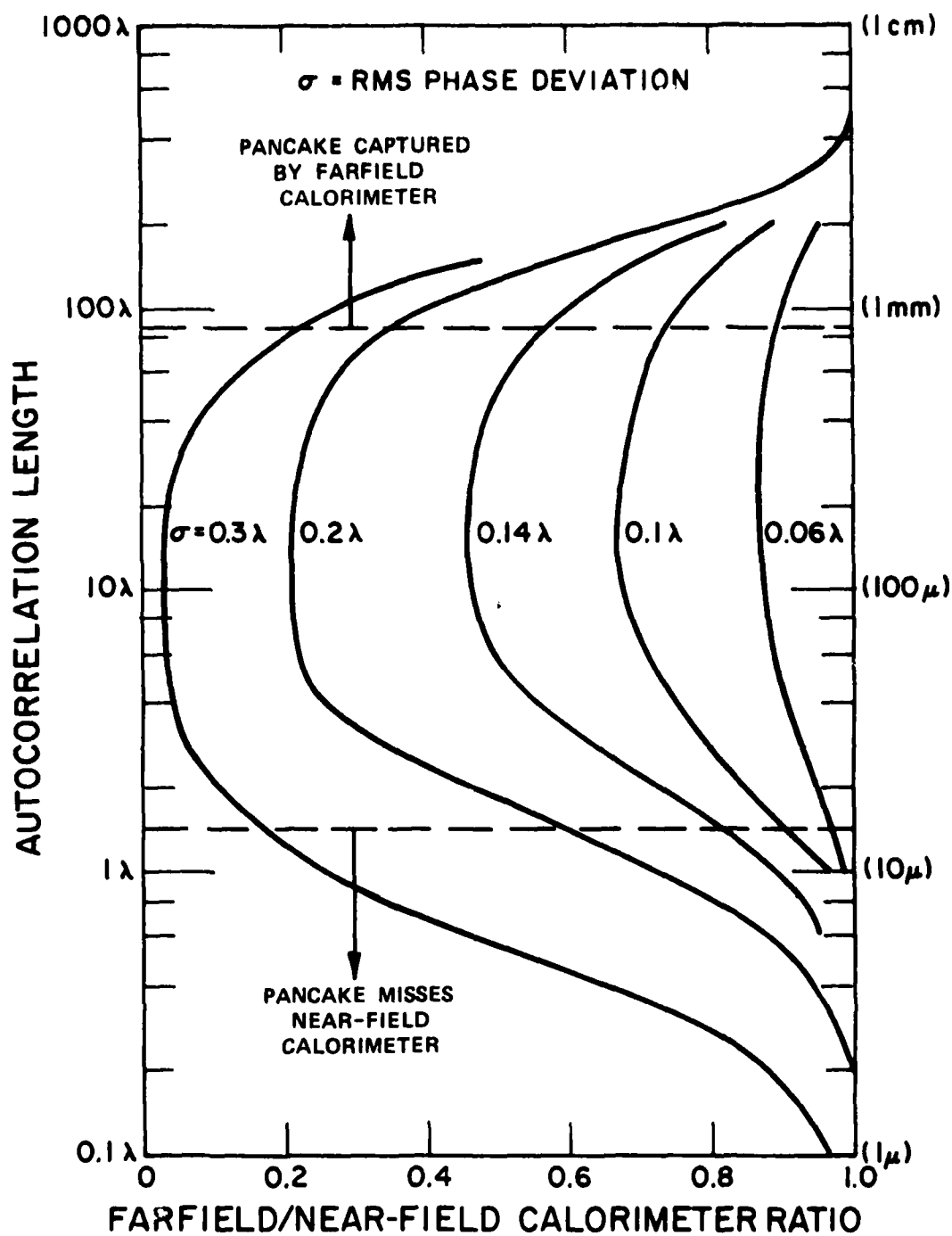
Figure 14 shows the energy transfer ratio that would be measured for a given RMS phase deviation,  $\sigma$ , as the autocorrelation length,  $a$  (scale size), is varied. Three regimes are apparent. For autocorrelation lengths in the range of  $10 \mu\text{m}$  to  $1 \text{ mm}$ , the wide-angle pancake is too large to be significantly intercepted by the farfield calorimeter, but does get collected in the near field. This is the way the experiment was designed to function. For very small scale sizes ( $\leq 10 \mu\text{m}$ ), the angular spread is too large for the pancake to be completely captured by the near-field calorimeter, and an erroneous value of  $\eta$  results. On the other hand, as the turbulence scale size increases past about  $1 \text{ mm}$ , the size of the pancake becomes comparable to that of the farfield calorimeter, and by definition the pancake ceases to exist.

For the ABEL experiments, then, if the observed energy transfer ratio is due to scattering from random turbulence, the autocorrelation length of such turbulence must lie in the range of about  $0.01$  to  $1.0 \text{ mm}$ . We will return to this point in the discussion of the interferometry results, Section 4.5.

## 4.2 FARFIELD/NEAR-FIELD TIME-RESOLVED INTENSITY

### 4.2.1 Experimental Issue

A knowledge of whether or not the energy transfer ratio varies appreciably during the laser pulse would help identify the responsible physical mechanism(s).



J9247

Figure 14. Turbulence Scale Size and Measured Energy Delivery Ratio

#### 4.2.2 Data

Simultaneous measurements of near- and farfield  $I(t)$  were obtained for five data shots, all from 30 January 1981. For these shots the resonator was in a centered-obscuration configuration.

Oscilloscope traces are shown on Figure 15. The near-field trace is on top in all the pictures; the slight fuzzing of the farfield trace was a defect in the oscilloscope. The apparent signal at 10-12  $\mu s$  is noise pickup from the sustainer discharge; lasing starts at about 15  $\mu s$ . Gain switch spikes are evident on all the traces. Since we only were interested in the shape of the traces, the vertical axis was uncalibrated.

The ABEL oscilloscope traces clearly show a decrease toward the end of the pulse, for four of the five data shots. For one of them (run #7), there may be some rolloff, but the trend is less distinct.

#### 4.2.3 Discussion

A possible interpretation of the  $I(t)$  data is that the far-field spot was deflecting as a function of time, rather than simply diminishing. The alignment requirements of the farfield  $I(t)$  detector were such that movement of the focal spot by an amount equal to its diameter would considerably reduce the signal. There is some evidence from the IR photographs (Section 4.3) that this may be happening.

If  $\eta$  truly was time dependent, on the other hand, the mechanisms discussed in Section 4.1 must be reconsidered since they do not directly include such time dependence. The diffraction structure should stabilize in a time comparable to the gain switch spike, and should not change thereafter. It is difficult to envision any way that laser gas would move into the beam path on a microsecond time scale. It is also hard to see how the turbulence strength could change (because of flow) within the pulse length. One possibility is that small hot spots in the beam give rise to localized pressure waves, which would grow as the laser pulse progresses. Since the scale size required is small, such waves could expand a significant amount on the time scale of a laser pulse. The mechanism would essentially constitute an open-loop Mode-Medium Interaction (MMI). Another possibility is edge waves initiated at the boundaries of the pumped gas. For 3:1:0.08 gas such waves propagate with an average velocity of  $\sim 0.04$  cm/ $\mu s$ . With the end of lasing occurring at  $\sim 20$   $\mu s$  after the start of pumping, such waves will have moved 0.8 cm into the mode cross-section area. We argue that the upstream and downstream boundaries are diffuse, and do not generate strong waves, whereas those at the anode and cathode are sharp. The area removed from the mode cross-section area is then  $(2)(0.8)(27)$  cm<sup>2</sup> = 43 cm<sup>2</sup>, or about 18% of the total. Clearly more analysis and experimentation are necessary to resolve this issue.

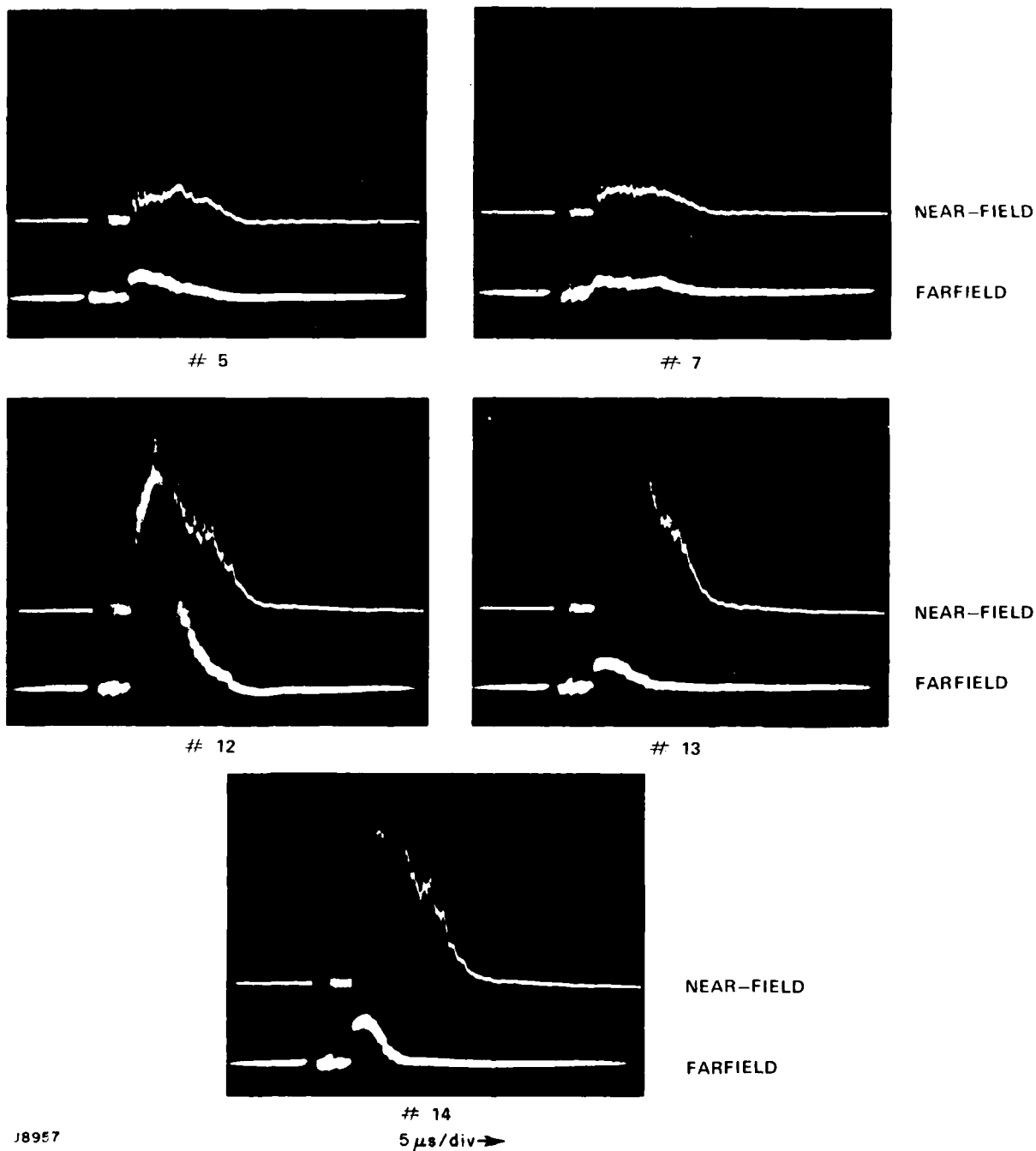


Figure 15. Near-Field and Farfield  $I(t)$  Traces for 30 January 1981

### 4.3 SPECIMEN 10.6 $\mu$ m IR PHOTOGRAPHS

#### 4.3.1 Experimental Issue

As we have seen, phase distortions larger than about 1 mm do not scatter light past the farfield calorimeter. Rather, they redistribute light within the solid angle subtended by the calorimeter, and lead to distortions of the observed focal spot. By observing qualitative features of these focal spots, one can hopefully deduce features of the original wavefront exiting the laser.

#### 4.3.2 Data

A total of 20 IR photographs were taken during the experimental period; we include here prints of seven of the most illustrative, Figures 16 through 22. Figures 19 through 22 will be discussed quantitatively in Section 4.4, where beam quality XDL numbers will be calculated. On each photo is a drawing of 10%-of-peak iso-contour lines indicating how a perfect focal spot would appear. The functions generating these curves are derived in Appendix A.

The location of the focal spot on each plate was observed to vary somewhat from shot-to-shot, justifying the original choice of a large-area photographic recording medium. The wander was generally of the order of 1-2 diffraction spot sizes.

#### 4.3.3 Discussion

Figures 16 through 18 were taken when the resonator was in a centered-obscuration configuration. The figures are in order of increasing apparent beam quality.

In Figure 16 the pattern resembles a series of horizontal stripes, without an obvious central spot. The vertical separation of these stripes agrees reasonably well with the lobe size and spacing predicted by theory ( $\sim 0.8 f\lambda/D_y$ ), indicating that optical quality in the flow direction is reasonably good. The smeared-out horizontal structure (or lack of structure) on the other hand, indicates that significant optical degradation exists, for this shot, in the anode-cathode direction. A possible interpretation of this picture, consistent with the  $I(t)$  results discussed in Section 4.2.2, is that the beam is being steered in the anode-cathode direction during lasing. This would require a mechanism for generating a time-dependent phase wedge. Another interpretation is that the anode-cathode direction aberration was not time varying, just severe.

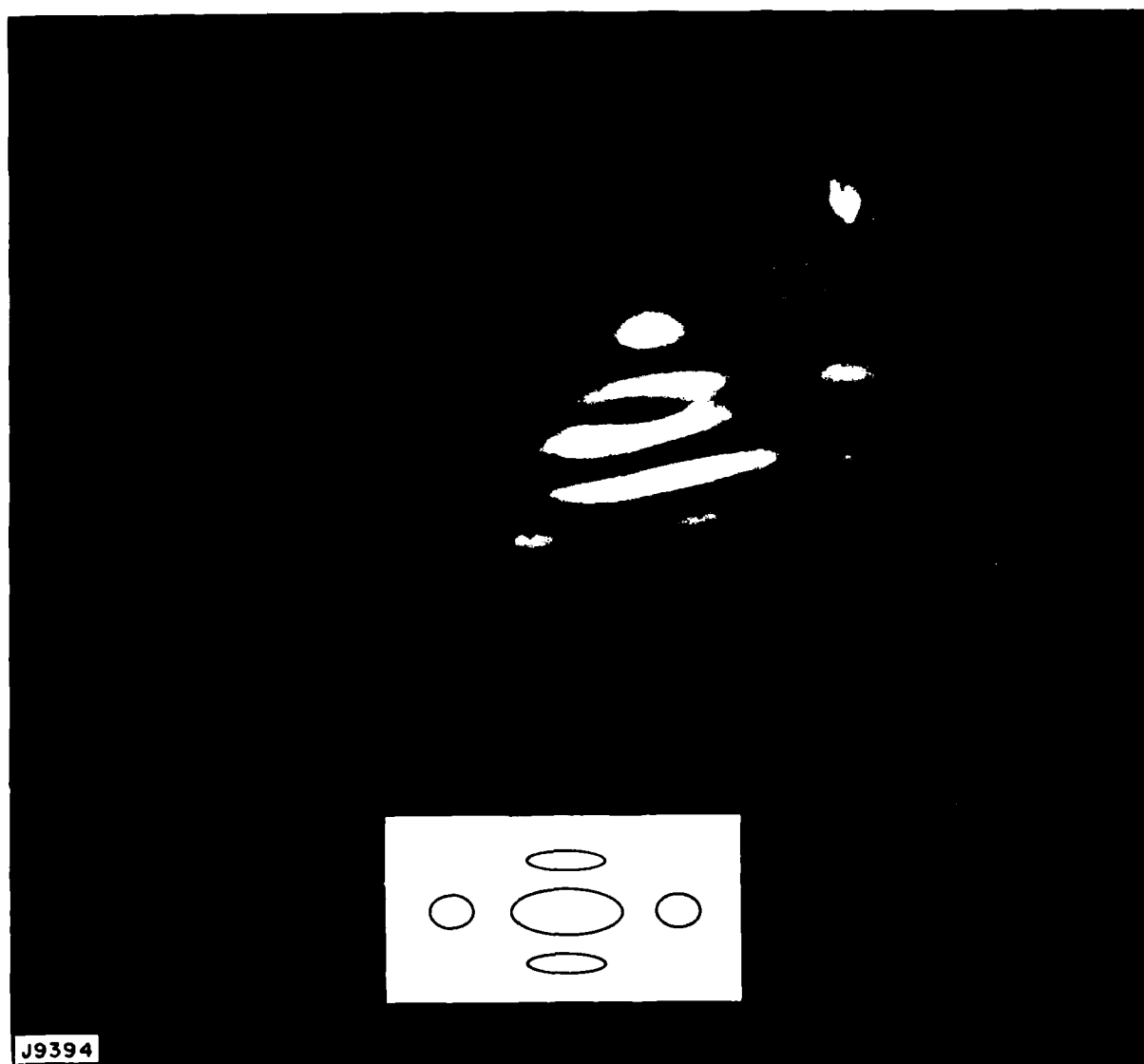


Figure 16. Focal Spot Infrared Photograph for Shot #11,  
30 January 1981

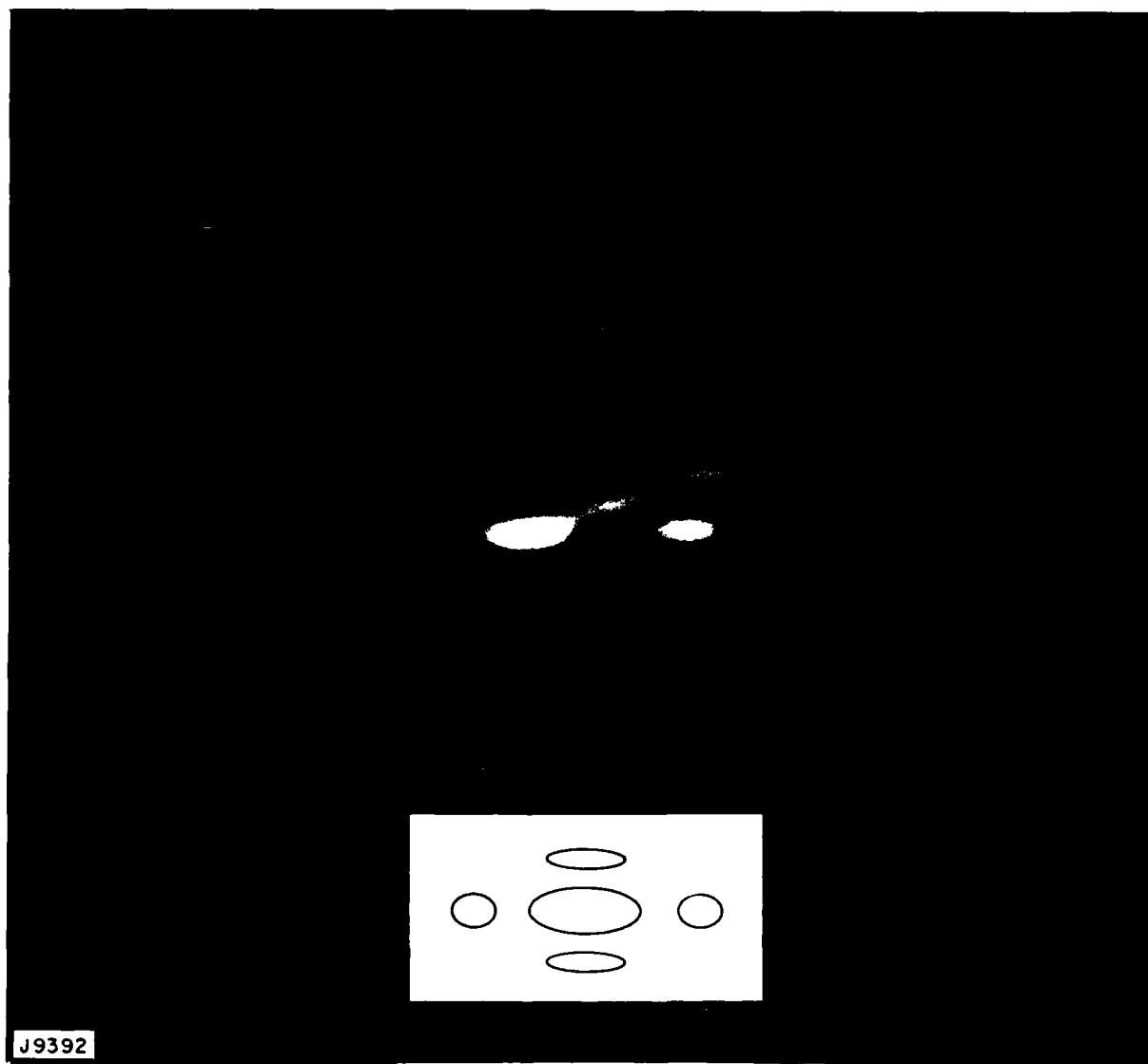


Figure 17. Focal Spot Infrared Photograph for Shot #4,  
29 January 1981



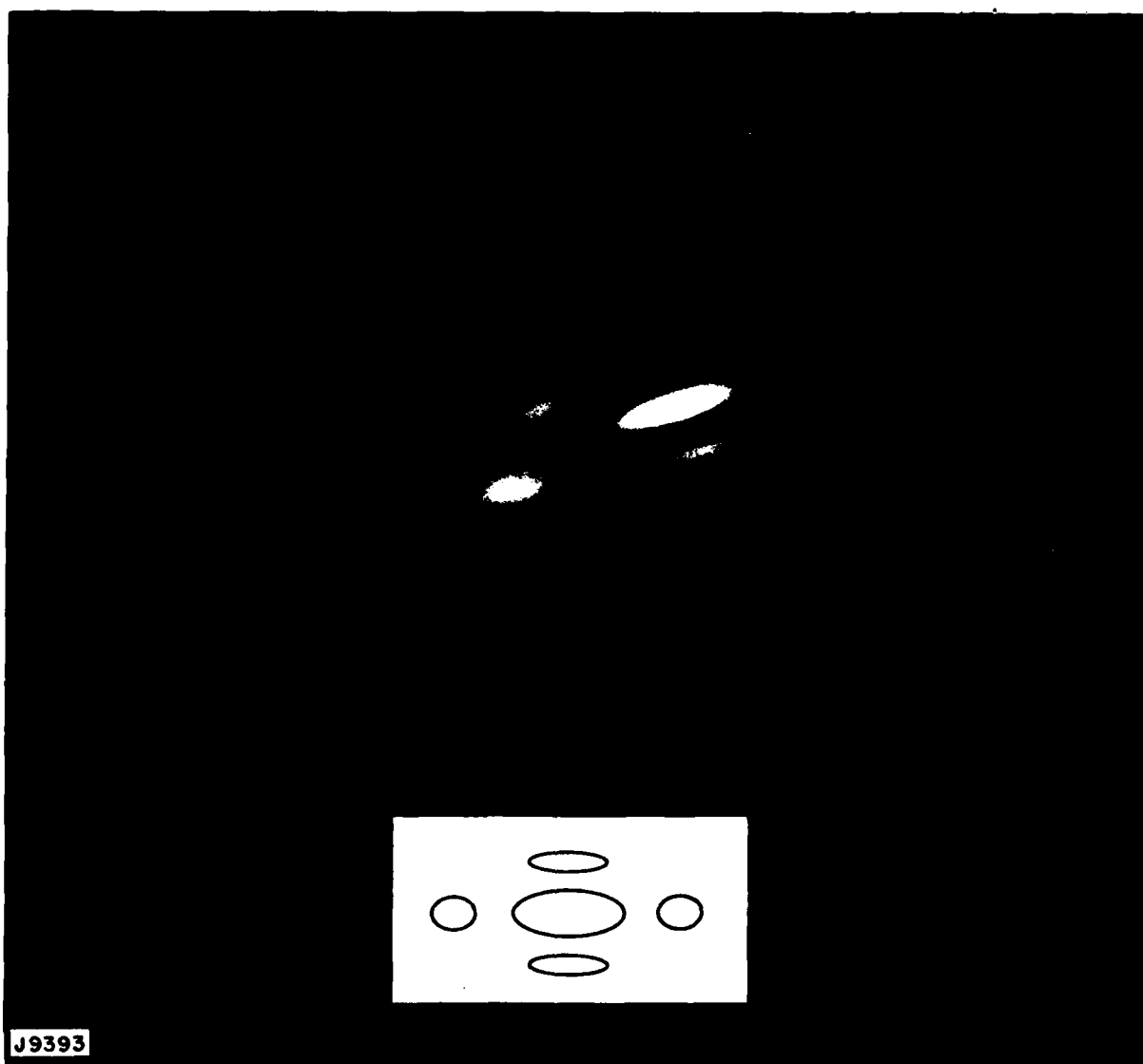


Figure 18. Focal Spot Infrared Photograph for Shot #2,  
30 January 1981

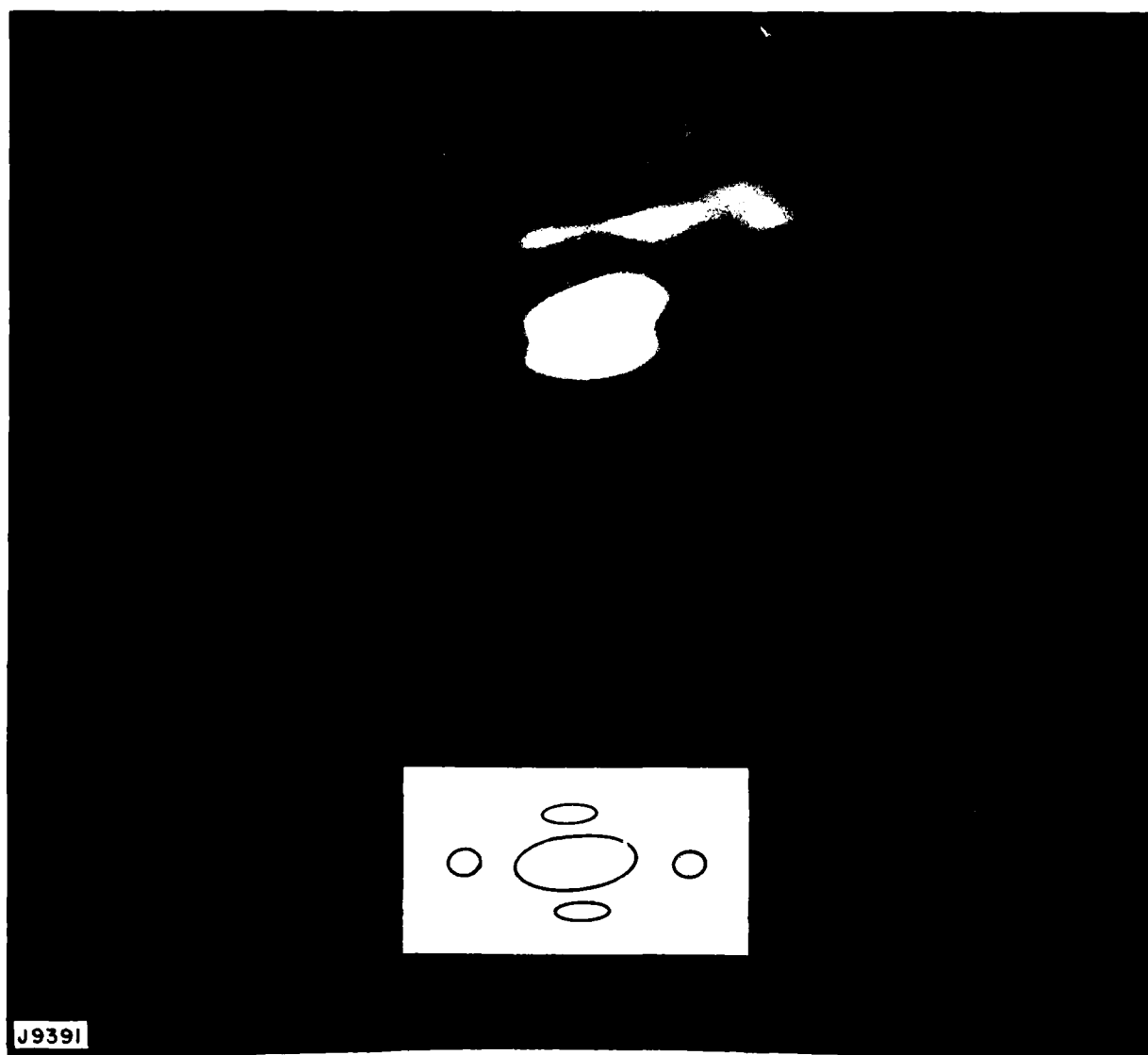


Figure 19. Focal Spot Infrared Photograph for Shot #4,  
2 February 1981

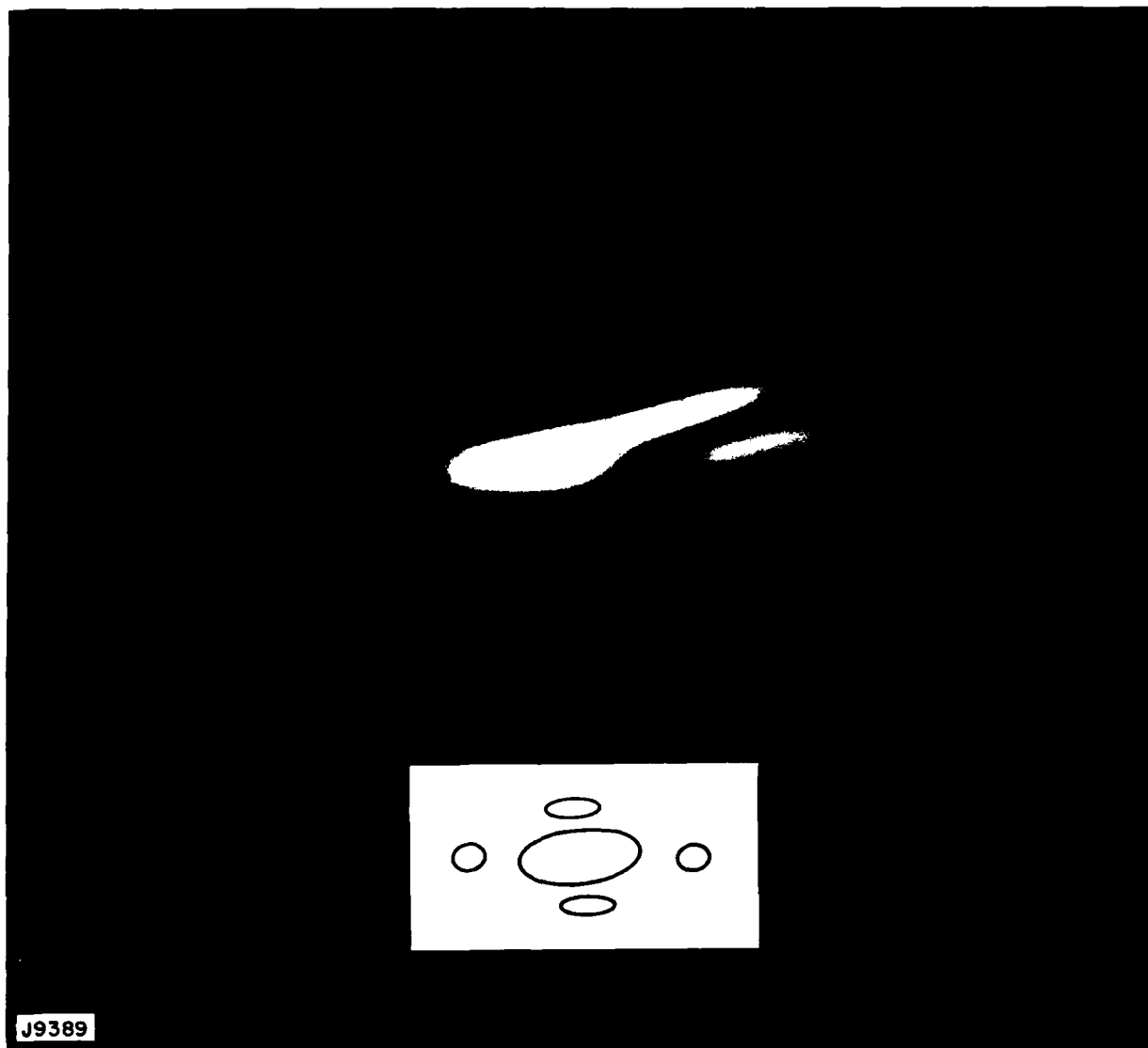


Figure 20. Focal Spot Infrared Photograph for Shot #13,  
31 January 1981

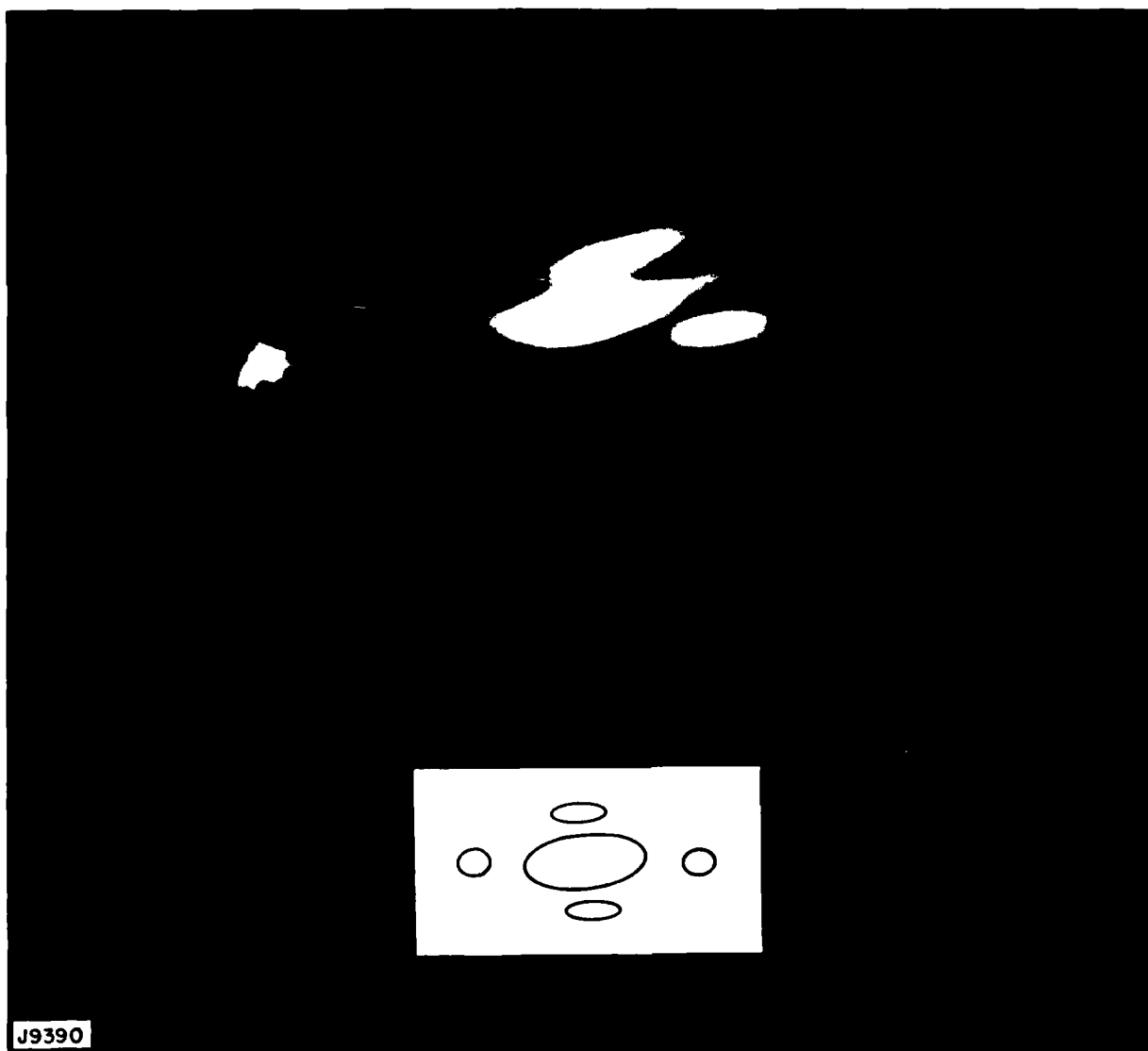


Figure 21. Focal Spot Infrared Photograph for Shot #3,  
2 February 1981

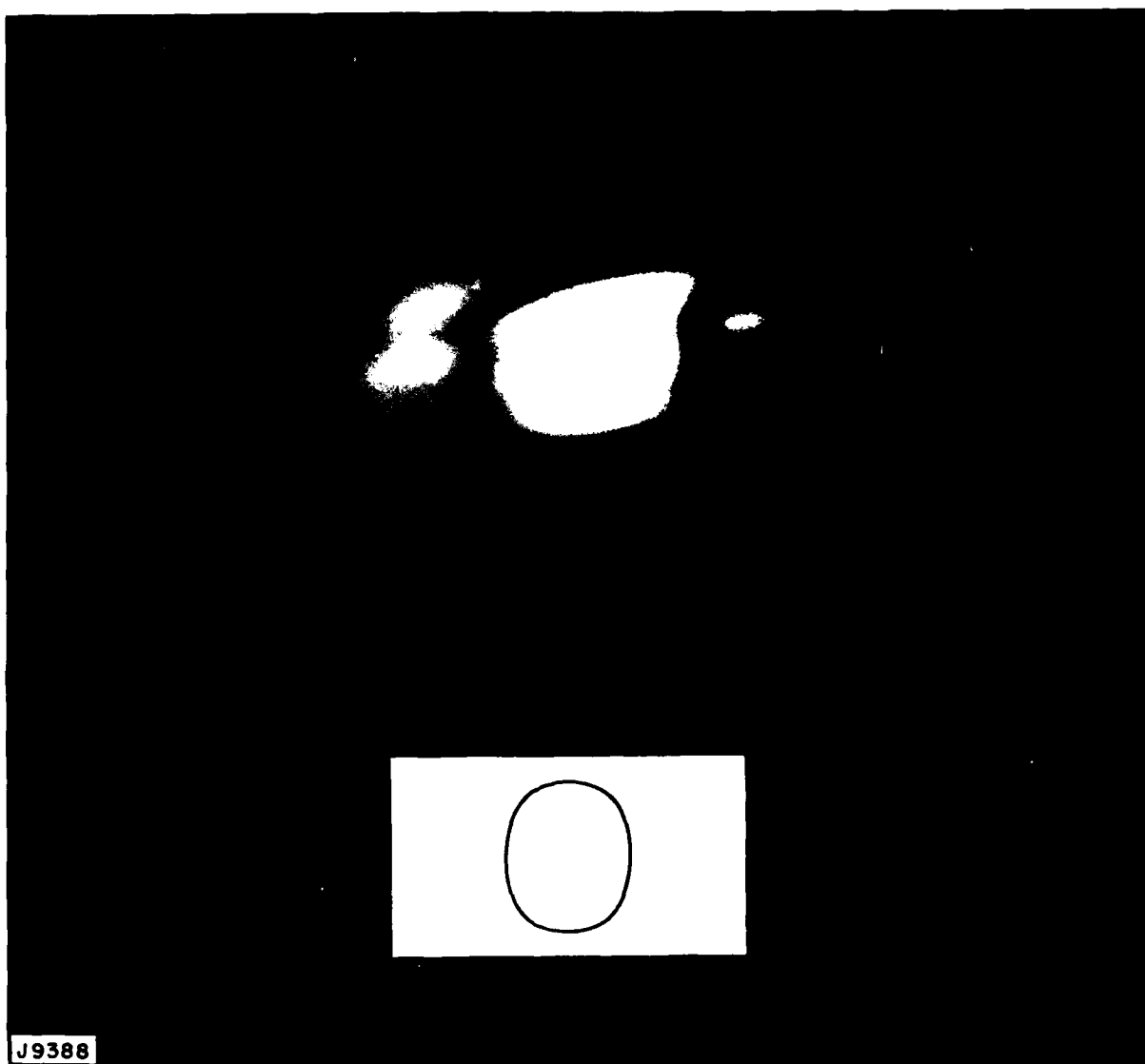


Figure 22. Focal Spot Infrared Photograph for Shot #7,  
2 February 1981

Figures 17 and 18 clearly represent better focal spots; the central peak is readily apparent, and the intensity of the higher order side lobes is reduced. This trend continues in Figures 19 and 20 which show focal spots for the off-center resonator configuration. As a group, the focal spot photographs of the off-center resonator appear to show better optical quality than those of the centered obscuration. This may indicate that mode control plays a role in the observed ABEL beam quality. (Centered resonators have mode separations that are more sensitive to very small tilt variations, if the effective Fresnel number is low enough.<sup>(6)</sup>)

The dominant feature of these pictures is the rotation or twist apparent in the central spot. This causes the brightest horizontal orders, lying to either side of the central spot, to be offset vertically from one another.

We have simulated this effect by artificially aberrating wavefronts in a commercial optical design computer program.<sup>(7)</sup> In order to successfully recreate the qualitative features seen in the pictures, it was sufficient to add astigmatism, but astigmatism oriented along new axes at 45° to the axes of the resonator. In other words, instead of a phase aberration of form

$$\phi_1(x,y) \sim \exp \left[ \frac{ik}{2L} (x^2 - y^2) \right] \quad (14)$$

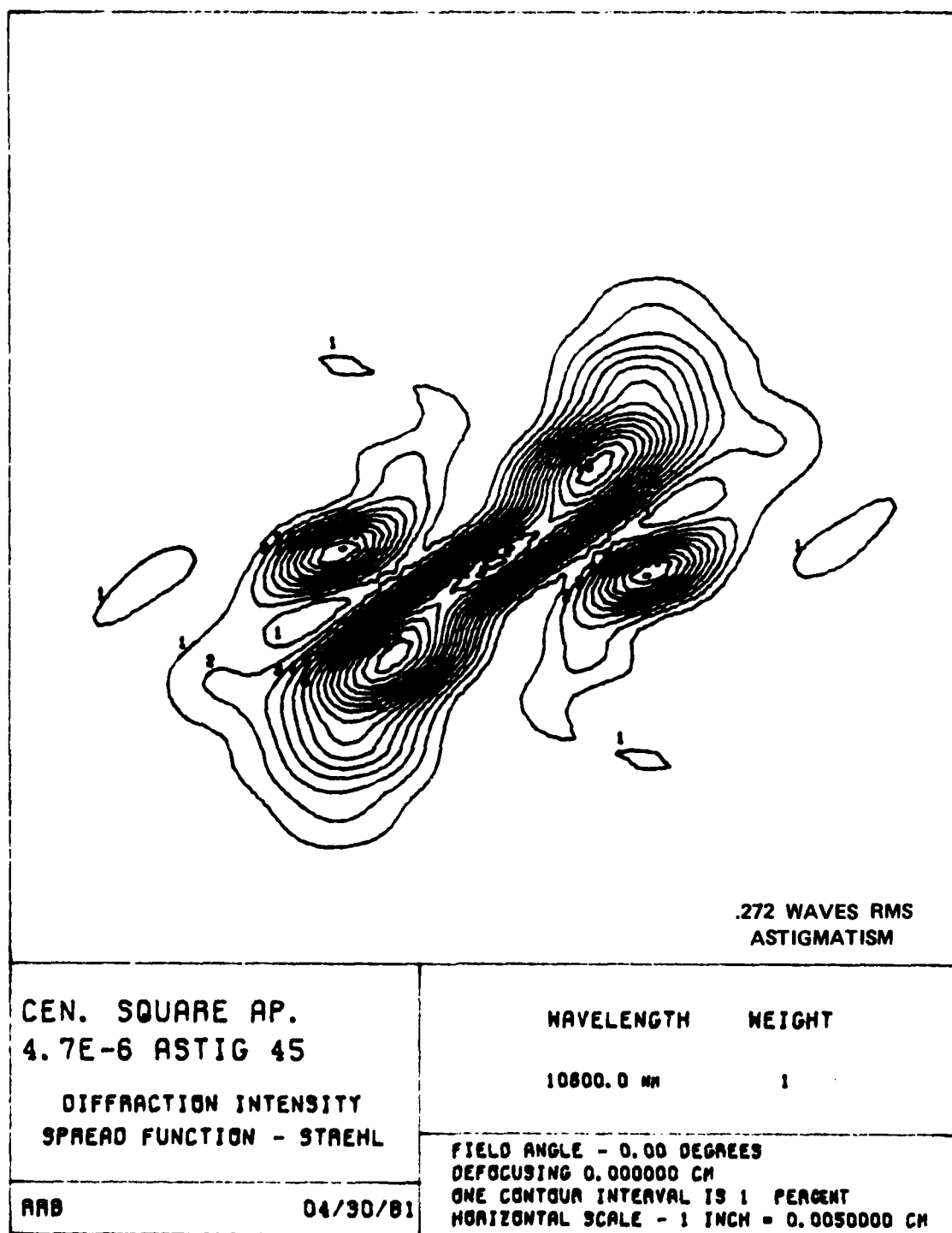
one of form

$$\phi_2(x,y) \sim \exp \left[ \frac{ik}{2L} (xy) \right] \quad (15)$$

was needed. Figures 23 through 25 (and Figure 26 for comparison) are computer calculated intensity contours of the farfield spots resulting from  $\phi_2$  aberrations of strength 0.272, 0.174, and 0.116 RMS waves, respectively. The diagonally-oriented distortion induced by  $\phi_2$  is quite evident. Astigmatism aligned with the resonator axes and coma were tried as synthesized aberrations but could not reproduce the observed twist of the central lobe. Strehl intensities for these cases (not allowing for any additional aberration) are 0.15, 0.25 and 0.58, corresponding approximately to the range actually seen on the photographs. By adding in lesser amounts of higher-order aberrations to the computer calculations, one could recreate the smaller-scale details, if desired.

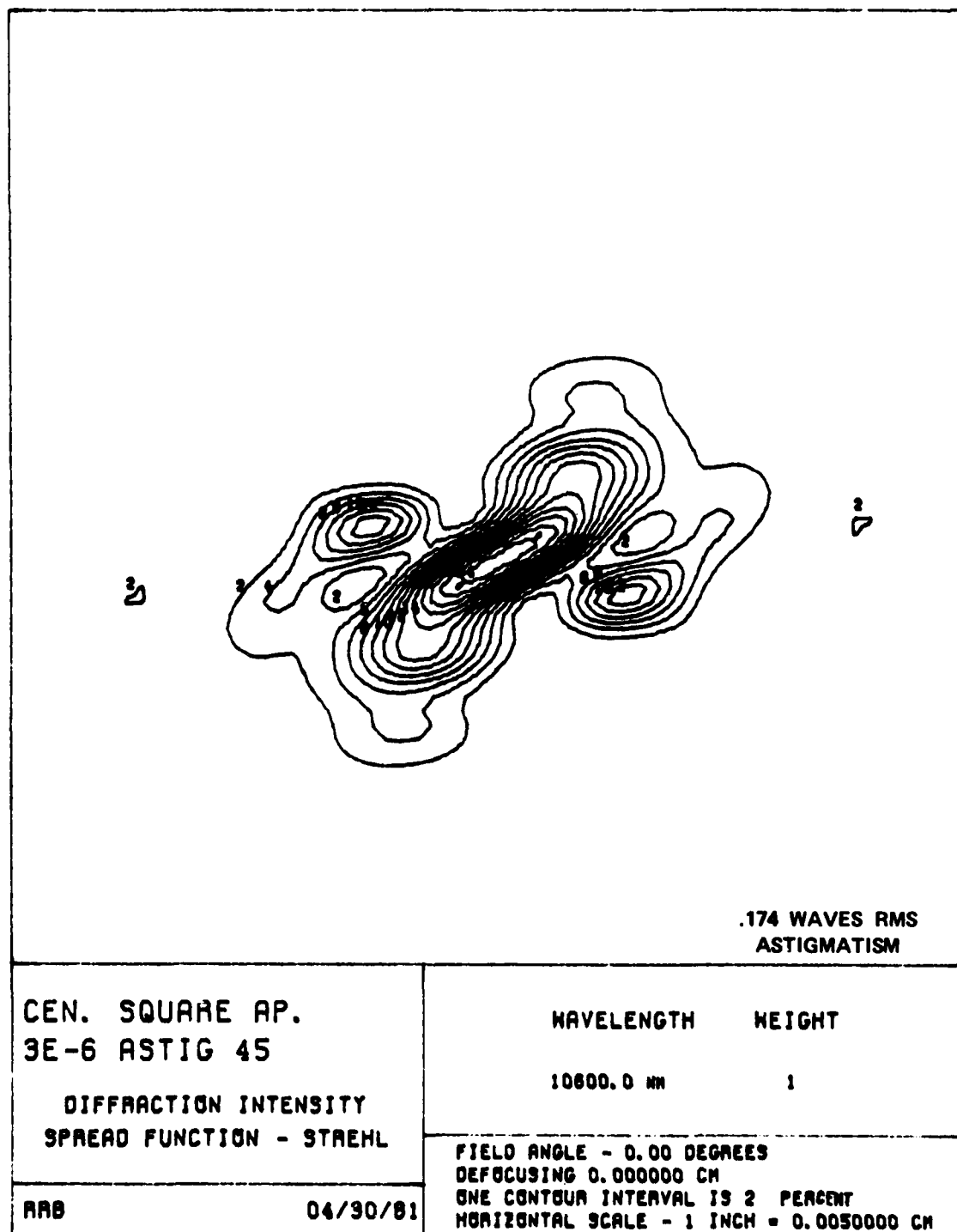
6. Weiner, M., Applied Optics 18, 11 (1 June 1979), pp. 1828-1834.

7. CODE V, Optical Research Associates, Pasadena, CA.



J9368

Figure 23. Calculated Focal Spot Intensity Contours for Astigmatism with Axes at 45° to Resonator Axes; Aberration Strength = 0.272 Waves RMS



J9370

Figure 24. Calculated Focal Spot Intensity Contours for Astigmatism with Axes at 45° to Resonator Axes; Aberration Strength = 0.174 Waves RMS





.116 WAVES RMS  
ASTIGMATISM

DECEN. SQUARE AP.  
2E-6 ASTIG 45

DIFFRACTION INTENSITY  
SPREAD FUNCTION - STREHL

WAVELENGTH HEIGHT

10600.0 NM 1

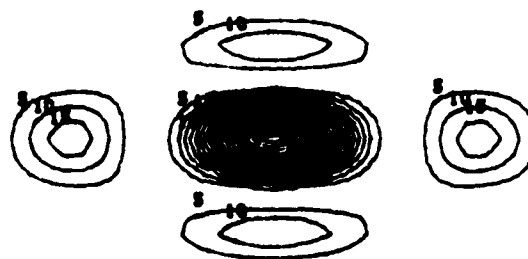
RRB

04/30/81

FIELD ANGLE - 0.00 DEGREES  
DEFOCUSING 0.000000 CM  
ONE CONTOUR INTERVAL IS 5 PERCENT  
HORIZONTAL SCALE - 1 INCH = 0.0050000 CM

J9371

Figure 25. Calculated Focal Spot Intensity Contours for  
Astigmatism with Axes at 45° to Resonator Axes;  
Aberration Strength = 0.116 Waves RMS



0 WAVES RMS  
ASTIGMATISM

CEN. SQUARE AP.  
PERFECT LENS

WAVELENGTH

HEIGHT

10800.0 NM

1

DIFFRACTION INTENSITY  
SPREAD FUNCTION - STREHL

FIELD ANGLE - 0.00 DEGREES

DEFOCUSING 0.000000 CM

ONE CONTOUR INTERVAL IS 5 PERCENT

HORIZONTAL SCALE - 1 INCH = 0.0050000 CM

RRB

04/30/81

J9369

Figure 26. Calculated Focal Spot Intensity Contours for Perfect Beam; Compare to Figures 23 through 25

Determination of the physical source of this astigmatism, without further measurements on ABEL, is difficult. As will be seen in Section 4.5, it is not evident in the flow interferograms. Examination of the various mirrors at the conclusion of the experiments failed likewise to show any indication of this type of aberration.

However, the identification of a simple low-order aberration as the cause of much of the apparent focal spot distortion is a very important observation. Even if the physical source of the astigmatism cannot be readily remedied, the aberration itself is easily corrected with external optics. By implication, then, the XDL numbers calculated in the following section may be viewed as constituting "worst case" values, amenable to significant improvement. Further, as will be seen in the following section, the effect of this astigmatism on the times-diffraction-limited number, when calculated by the encircled energy method, is rather small.

#### 4.4 BEAM QUALITY CALCULATIONS

##### 4.4.1 Experimental Issue

Beam quality is not an unambiguous physical parameter like, say, length or voltage but rather is subject to a number of definitions depending on the perspective of those doing the defining. For ABEL we calculate two beam quality times-diffraction-limited (XDL) numbers that are widely used.

##### 4.4.1.1 Strehl Ratio XDL

Those approaching the question of laser beam quality from the viewpoint of optical systems analysis often think in terms of peak focal spot irradiance. The ratio of the observed focal spot peak irradiance to that expected for a perfect beam is called the Strehl ratio (SR):

$$SR = \frac{\text{observed } I}{\text{ideal } I} \quad (16)$$

The ideal focal spot peak irradiance is calculated (Refer to Appendix A) assuming a uniform plane wave illumination of the laser output aperture. Though the feedback mirror size (i.e., output coupling) affects the absolute focal spot intensity by changing the near field area, that effect is generally normalized out of the calculation as we have done in Eq. (A9).

The Strehl ratio XDL number is then:

$$SR \text{ XDL} \equiv 1/(SR)^{1/2} \quad (17)$$

Another reason for the use of the Strehl ratio XDL is that it may in principle be calculated from interferograms. If we assume for the moment that flow distortion is the dominant factor affecting beam quality, then a single pass interferogram showing  $\phi_{\text{RMS}}$  waves of distortion will lead to a laser beam Strehl ratio of about

$$\exp[-2(2\pi\phi_{\text{RMS}})^2]$$

providing  $\phi_{\text{RMS}}$  is not too large.

#### 4.4.1.2. Encircled Energy XDL

The user community associated with beam propagation and target interaction often uses beam quality in the sense of the amount of energy within some defined area (i.e., bucket) at the focal plane, compared to how much would be there for a perfect beam. More formally, if  $F_{\text{th}}$  and  $F_{\text{obs}}$  are the theoretical and observed farfield fluence (energy/unit area) distributions, then the encircled-energy XDL is defined by

$$(\text{Encircled Energy XDL})^2 = \frac{\iint_B F_{\text{th}} dA}{\iint_B F_{\text{obs}} dA} \quad (18)$$

where the area integral is carried out over the specified bucket, B. The numerical answer calculated for a given real beam depends on the choice of bucket size and shape. For rectangular aperture lasers like ABEL, there are several plausible bucket choices:

- One "Airy rectangle" with dimensions  $\Delta x_0$  and  $\Delta y_0$  as defined by the outer dimensions  $D_x$  and  $D_y$  of the projected near-field mode;  $\Delta x_0 = 2 f\lambda/D_x$ ,  $\Delta y_0 = 2 f\lambda/D_y$ . For the full beam of unstable resonators, this bucket is somewhat larger than the apparent central spot in the farfield. For rectangular samples of the near field mode (of size  $D_x$  by  $D_y$ ), it is the same size.
- An Airy rectangle based on the first zeroes of the theoretical farfield pattern. For the 75% coupling ABEL resonator, the resulting bucket is 80-85% the size of the previous case, depending on whether the obscuration is centered or off-center.

- A non-rectangular bucket coincident in size and shape with the central farfield spot. This is a little different than the previous definition for the case of off-center obscuration resonators, as can be seen by careful comparison of the contour lines on Figures 16 and 19.

Other less often used definitions include strictly circular buckets, buckets out to the 50% intensity point, and buckets sized to encircle some given percentage of the energy. For the present calculations, we use the second method above to determine encircled energy XDL.

The Strehl ratio and encircled energy XDL calculations do not in general yield the same results, even allowing for experimental error. The relationship between the two depends on the nature of the aberrations present. For example, it can be shown that for defocus,\* the two XDL numbers are about the same, whereas for astigmatism (Refer Appendix B) the Strehl-derived XDL turns out to be the square of the encircled-energy XDL.

#### 4.4.2 Data

We have selected four IR photographs for detailed analysis and beam quality calculation, representing the best focal spots. In order to facilitate data reduction and present the focal spots in a more graphic way, the film plates were scanned by an Isodensitracer which, as its name suggests, produces contour maps of the photographic image density. By keying in the calibrated IR film response, the Isodensitracer produces vivid false-color maps of fluence distributions from which  $\text{J}/\text{cm}^2$  values may be read directly. Figures 27 through 30 are the false-color fluence distribution maps for the four best focal spots.

Several features of these maps should be mentioned. The light green corresponding to the 0 to  $0.1 \text{ J}/\text{cm}^2$  range and the dark green of the  $0.1$  to  $0.2 \text{ J}/\text{cm}^2$  range are each divided into six subcontours, with the explicit fluence resolution thus  $0.017 \text{ J}/\text{cm}^2$ . Ultimate resolution depends of course on film grain noise; one may estimate from the appearance of the contours that it is at most  $0.005 \text{ J}/\text{cm}^2$ . Figures 29 and 30 show the presence of a very gradual ramping of the background film density, due to a slight nonuniformity in the intensity of the narrow band visible illumination. This has to be taken into account in the encircled energy integration. Finally, it will be noticed that

\* See Reference (1), Born & Wolf, Ch. 8. Strehl XDL may be computed from their Eq. (8-26) for normalized defocus distance  $u$ ; encircled energy XDL is computed from Figure 8-43 by noting the encircled energy at points  $(u, v = 3.83)$  compared to  $(0, v = 3.83)$ .  $v = 3.83$  is the Airy dark ring radius in units of  $1.22 \pi$ .

SHOT # 7 2 FEB 1981



J9933

1 cm

DIFFRACTION SPOT SIZE = 1.39 cm x 1.17 cm

Figure 27. Fluence Map of ABEL Focal Spot

SHOT # 3 2 FEB 1981



K1587

DIFFRACTION SPOT SIZE = 1.00 cm x .44 cm

Figure 28. Fluence Map of ABEL Focal Spot (Shading at Left is a Background Artifact)

SHOT # 13 31 JAN 1981

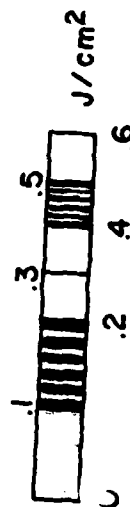


Figure 29. Fluence Map of ABEL Focal Spot

K1589



SHOT # 4 2 FEB 1981



1 cm

DIFFRACTION SPOT SIZE = 1.00 cm x .44 cm

Figure 30. Fluence Map of ABEL Focal Spot

K 1588

the fluence distribution maps are mirror images of the actual IR photos; this is merely an artifact induced by the way the Iso-densitracer scans the film plate.

Putting the fluence distribution into a contour map format simplifies evaluation of the encircled energy integrals. Rather than forming the two-dimensional integral

$$E(\text{bucket}) = \iint_B F(x,y) dx dy \quad (19)$$

we instead measure the area  $A(F_i)$ , associated with the  $i^{\text{th}}$  value of fluence, that lies within the limits of both the bucket and the  $F_i$  contour. This is easily done by any number of planimetry techniques. Then we just have the one-dimensional integral

$$E = \int A(F) dF \quad (20)$$

Such an integral can be visualized as taking horizontal rather than vertical slices through the surface  $F(x,y)$ .

#### 4.4.3 Discussion

We will calculate in detail the results for one picture, and tabulate the results (calculated in the same way) for the other three.

##### 4.4.3.1 Analysis of Shot #7, 2 February 1981

For this shot, the resonator was in the off-center configuration. The top part of the beam was blocked off in the near-field, as shown in Figure 31, with the lower, nearly square, portion of area  $121.4 \text{ cm}^2$  allowed to propagate to focus. Since there was no obscuration in that part of the beam, its theoretical farfield pattern is just the simple expression of Eq. (A4) (See Appendix A).

#### Strehl Ratio XDL

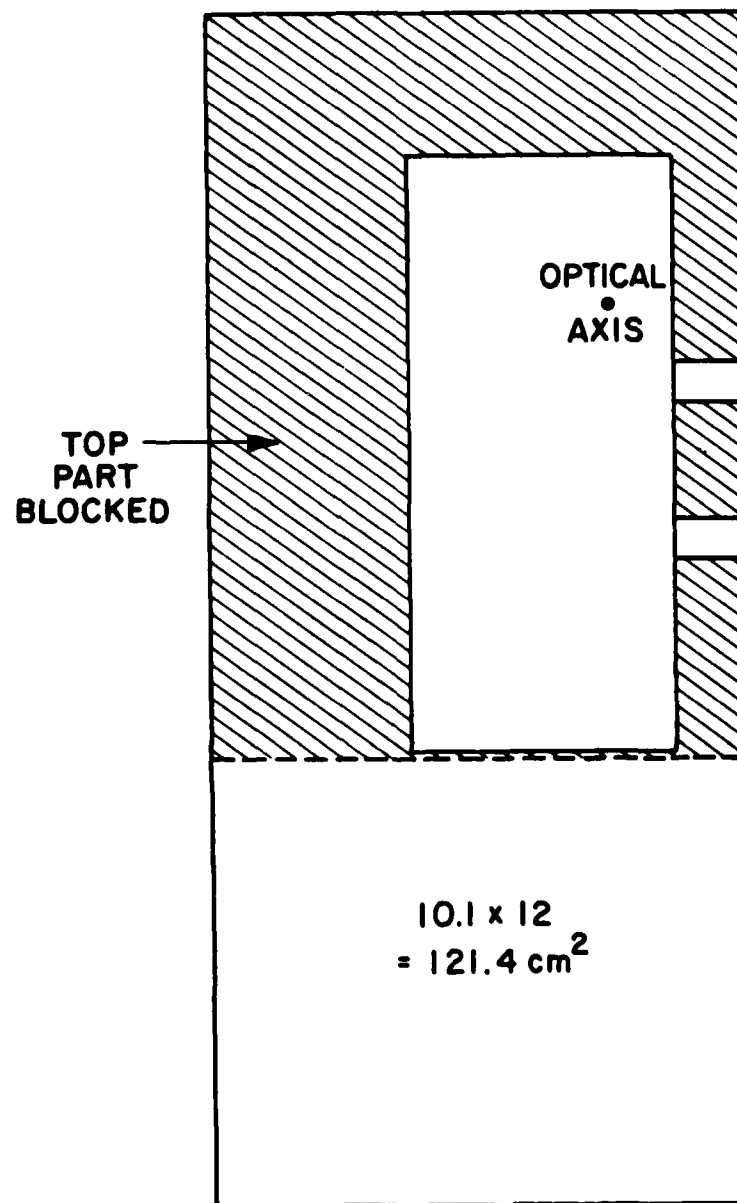
The theoretical peak farfield fluence,  $F_{th}$ ,

$$= (\text{near-field fluence}) \cdot (\text{N.F. area} / f)^2 \quad (\text{system losses})$$

System losses are:

- attenuators
- mirror reflectivity
- energy delivery ratio,  $\eta$

RESONATOR CONFIGURATION  
FOR  
SHOT #7 2 FEB 81



J9251

Figure 31. Rectangular Near-Field

Then for this shot we have

$$F_{th} = \left( \frac{2780 \text{ J}}{241 \text{ cm}^2} \right) \cdot \left( \frac{121.4 \text{ cm}^2}{6650 \text{ } 0.00106 \text{ cm}^2} \right)^2 \cdot (0.024) \text{ screen C} \\ \cdot (0.985)^3 \cdot (0.039) \cdot (0.73) = 2.23 \text{ J/cm}^2 \\ \begin{array}{ccc} \nearrow & \nearrow & \nearrow \\ \text{3 mirrors} & \text{salt} & \eta \end{array}$$

For this shot, there was no second attenuator screen. From the fluence distribution map the peak observed fluence was apparently about 1.5 J/cm<sup>2</sup>, whence

$$\text{Strehl XDL} = (2.23/1.5)^{1/2} = 1.22$$

#### Encircled Energy XDL

For a simple rectangular aperture, the farfield bucket size is just

$$\Delta x_0 = \frac{2 f \lambda}{D_x} = \frac{2(6650 \text{ cm})(0.00106 \text{ cm})}{12 \text{ cm}} = 1.17 \text{ cm}$$

$$\Delta y_0 = \frac{2 f \lambda}{D_y} = \frac{2(6650 \text{ cm})(0.00106 \text{ cm})}{10.1 \text{ cm}} = 1.39 \text{ cm}$$

The total energy deposited on the IR film is proportional to that on the farfield calorimeter:

$$E_{tot} = \frac{E(\text{f.f. calorimeter})}{\text{salt transmission}} \cdot (\text{salt reflectivity}) \\ = \frac{21.3 \text{ J}}{1 - (2)(0.039)} \cdot (0.039) = 0.90 \text{ J}$$

One may also directly integrate all the fluence visible in the picture, although the above calculation is easier. The cases for which we have done it both ways show agreement to better than 10%. From Figure 32, 81.5% of the total energy on the film should be in the central spot, or  $E_{th} = (0.90 \text{ J}) \cdot (81.5\%) = 0.733 \text{ J}$ . The observed bucket energy, calculated from

$$E_{obs} = \int A(F) dF \quad (21)$$

is 0.505 J. Then

$$\text{encircled energy XDL} = (0.733/0.505)^{1/2} = 1.20$$

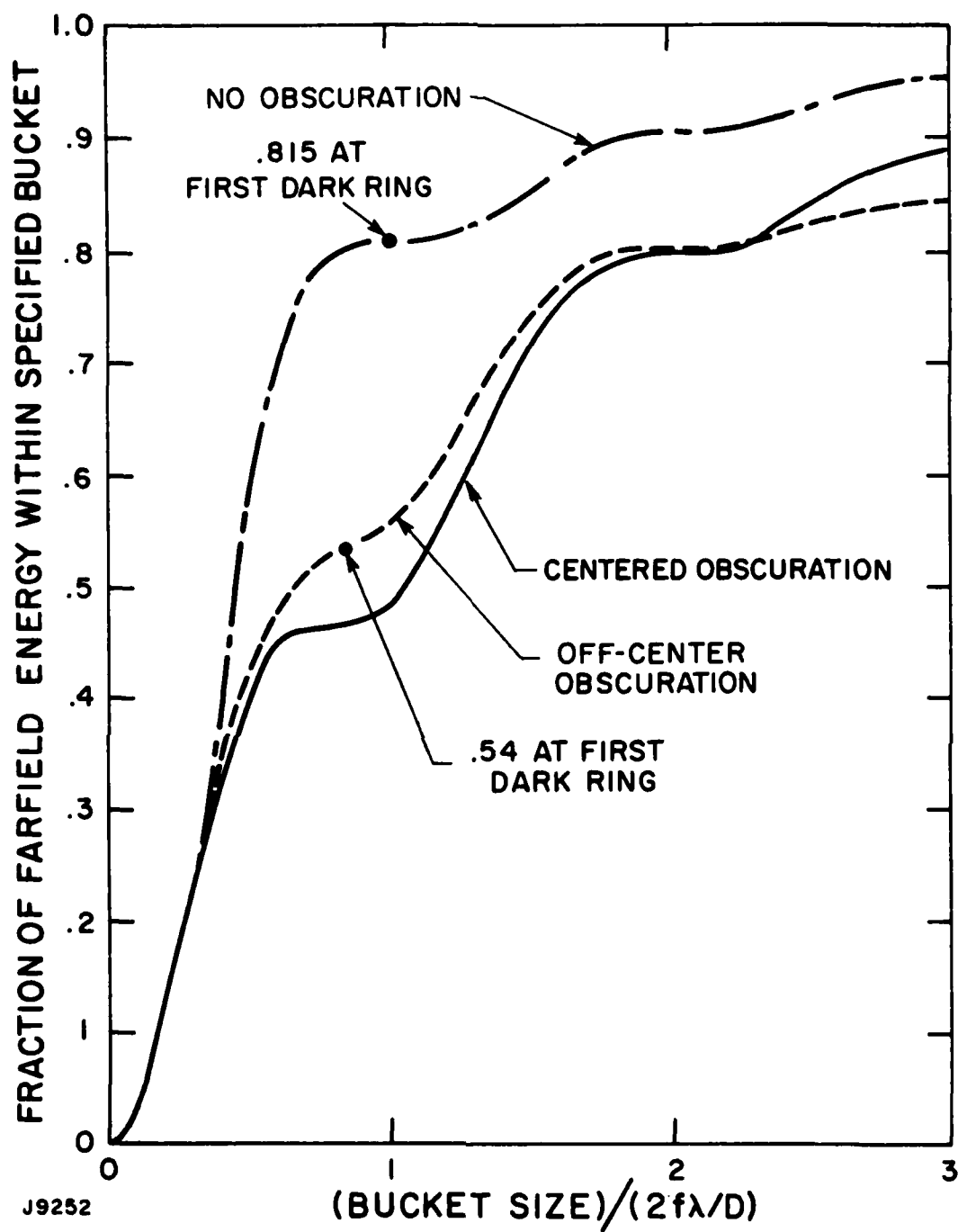


Figure 32. Theoretical Encircled Energy Ratios for the Various Resonator Configurations

#### 4.4.3.2 Tabulated XDL Values

We summarize in Table 2 the results for all four fluence distribution maps. The bucket for encircled energy XDL is the first "Airy disk" discussed in Section 4.4.1. Calculations for the last three were done the same way as the first, with the appropriate system loss factors used for each shot; the full aperture was focused for these last three cases. In particular:

- 1) Near-field area was  $241 \text{ cm}^2$ .
- 2) Expected energy fraction (see Figure 32) for the central spot of the off-center resonator was 54%.
- 3) A second screen (screen A) was used in the beam train.

For the last three tabulated shots, the encircled energy XDL values are distinctly lower than those computed from the Strehl ratio. This is entirely consistent with interpreting the dominant aberration to be astigmatism. For that idealized case, as we have shown, the one value is very nearly the square root of the other. The presence of other aberrations, and the uncertainty in the near-field energy (which enters into the Strehl calculation) are sufficient to produce the results seen in Table 2.

The first shot listed in the table does not initially appear to be consistent with the others since the Strehl and encircled energy XDL values are nearly identical. However, it will be noted from the Isodensitracer map and Figure 8 that the apparent peak fluence value of  $1.5 \text{ J/cm}^2$  was actually in the overexposure region where the film emulsion suffers overheating and resulting degradation. When the negative was processed, the calibration curve keyed into the Isodensitracer for fluences  $> 1.25 \text{ J/cm}^2$  was an extrapolation of that used for  $0.8$  to  $1.25 \text{ J/cm}^2$ . In actuality, a considerable variation of film response from picture to picture is observed at these high fluences (in contrast to excellent reproducibility at lower ones), with the extrapolated curve representing only an average. For this picture, the true peak fluence may well have been some lower value, say  $1.3 \text{ J/cm}^2$ . This would then make the results more consistent with the others. What all this says is that this particular picture was too overexposed to permit calculating an accurate Strehl ratio, though such overexposure has only a slight effect on the encircled energy calculation.

#### 4.5 INTERFEROMETRY RESULTS

##### 4.5.1 Experimental Issue

From an experimental standpoint, it is considerably easier to take cavity interferograms than to conduct detailed beam quality

TABLE 2. XDL VALUES

Day/Shot	Near-Field Energy (J)	$\eta$	Beam Sample	Strehl XDL	Encircled Energy XDL	Mass Flow Rate (lb/s)
2/2/81/#7	2780	0.73	50% of Near-Field	1.22	1.20	41.7
2/2/81/#3	2280	0.69	Full Aperture	1.40	1.25	25.8
1/31/81/#13	2770	0.50	Full Aperture	1.58	1.13	35.0
2/2/81/#4	2470	0.76	Full Aperture	1.76	1.25	38.9

measurements. Thus, assuming all or most beam degradation to be caused by flow inhomogeneities, there is a strong incentive to infer beam quality from interferometry results.

As is well known, the Strehl intensity of a focused beam can be related to the RMS phase content  $\phi_{\text{RMS}}(\text{near-field})$  by

$$\text{Strehl Ratio} = \exp\left(-\left[\frac{2\pi}{\lambda} \phi_{\text{RMS}}(\text{near-field})\right]^2\right) \quad (22)$$

In a resonator, where the light bounces back and forth before escaping, the one-pass phase aberration  $\phi_{\text{RMS}}(\text{one pass})$  is related to the net near-field phase  $\phi_{\text{RMS}}(\text{near-field})$  by some multiplier. Strictly speaking, this multiplier is different for the different scale-size components of  $\phi_{\text{RMS}}(\text{one pass})$ , but for a resonator magnification of 2 (the present case) a good approximation is that

$$\phi_{\text{RMS}}(\text{near-field}) = \sqrt{2} \phi_{\text{RMS}}(\text{one pass}) \quad (23)$$

so that

$$\text{Strehl Ratio} = \exp\left(-2\left[\frac{2\pi}{\lambda} \phi_{\text{RMS}}(\text{one pass})\right]^2\right) \quad (24)$$

In simplest terms, the main purpose of the interferometry subtask was to see if the above formula, when used with cavity interferograms representing the same flow conditions as were present during lasing, predicts the observed Strehl ratio XDL. We also wanted to see if the large-scale distortions (aberrations) calculated from the interferograms matched those observed in the IR photographs. The situation is somewhat more subtle, though, because in principle the interferogram should predict not only the Strehl ratio XDL, but also the energy transfer ratio,  $\eta$ , provided that its physical mechanism is small-scale size turbulence scattering.

#### 4.5.2 Data

A variety of interferograms were taken for full system flow, core plus end flow, and core flow only, for both low and high mass flow rates. For this report we have analyzed and will discuss only the worst case; namely, full system flow at high flow rate.



Interferogram reduction was carried out using the FRINGE computer code originally developed at the University of Arizona Optical Sciences Center. Two versions of this program were used. One, at AERL, has a relatively fine data mesh, but lacks the capability to fit the higher order aberration functions or to calculate a predicted focal spot pattern. The other version, at the Air Force Weapons Laboratory, has complementary capabilities. Unfortunately, no one has written a program combining fine-scale spatial resolution with comprehensive data analysis.

#### 4.5.3 Discussion

Figure 33 shows the "worst case" flow interferogram selected for analysis. For reference, Figure 34 is the corresponding tare picture. The chief features visible in the flow picture are the overall random irregularity, and the strong curvature developing at the downstream (top) edges.

Figure 35 shows a phase map reduction of the interferogram with a computer calculated (AERL version of FRINGE) RMS content of 0.075 waves. This is distributed as 0.016 waves RMS defocus, 0.003 waves of astigmatism, 0.001 waves of coma, and 0.055 waves of higher order aberration. The astigmatism computed here has axes nearly coincident with the symmetry axes of the resonator, and clearly is not the astigmatism evident in the focal spot photos. Using 0.075 waves of RMS phase distortion leads to a predicted Strehl ratio of

$$\exp [-2(2\pi \cdot 0.075)^2] = 0.64$$

and a predicted Strehl XDL of  $(0.64)^{-1/2} = 1.25$ . However, in the beam quality measurements the best focus was determined experimentally, so that a more appropriate phase distortion number is that obtained with focus effects removed, i.e.,  $0.075 - 0.016 = 0.059$  waves RMS whence

$$SR = \exp [-2(2\pi \cdot 0.059)^2] = 0.76$$

and

$$XDL(SR) = (0.76)^{-1/2} = 1.15$$

This result clearly is better than what was observed. It may well represent, though, the residual left if the unidentified astigmatism dominating the focal spot pictures is removed; this cannot be determined for certain, of course, without further experiment.

The AERL version of FRINGE admits up to 1000 wavefront samples. Thus the smallest feature discernible in the flow direction

11/21/80, RUN # 1

3N<sub>2</sub>:1CO<sub>2</sub> MIX

T<sub>g</sub> = 265°K

U<sub>c</sub> = 2.58 cm/ms

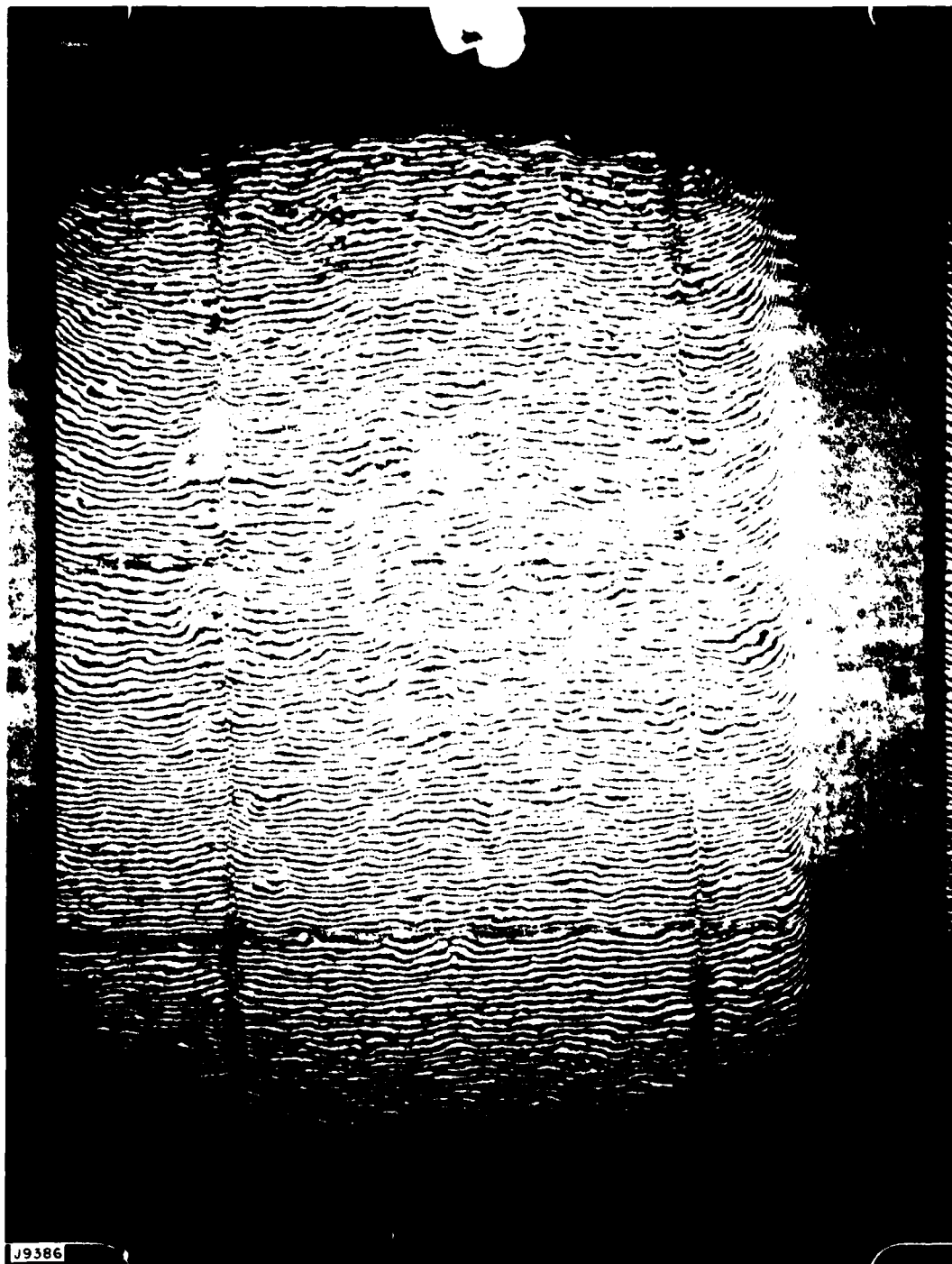


Figure 33. Full-System Flow ABEL Cavity Interferogram (No Energy Loading); Calculated  $I/I_0 = 0.76$

11/20/80, TARE

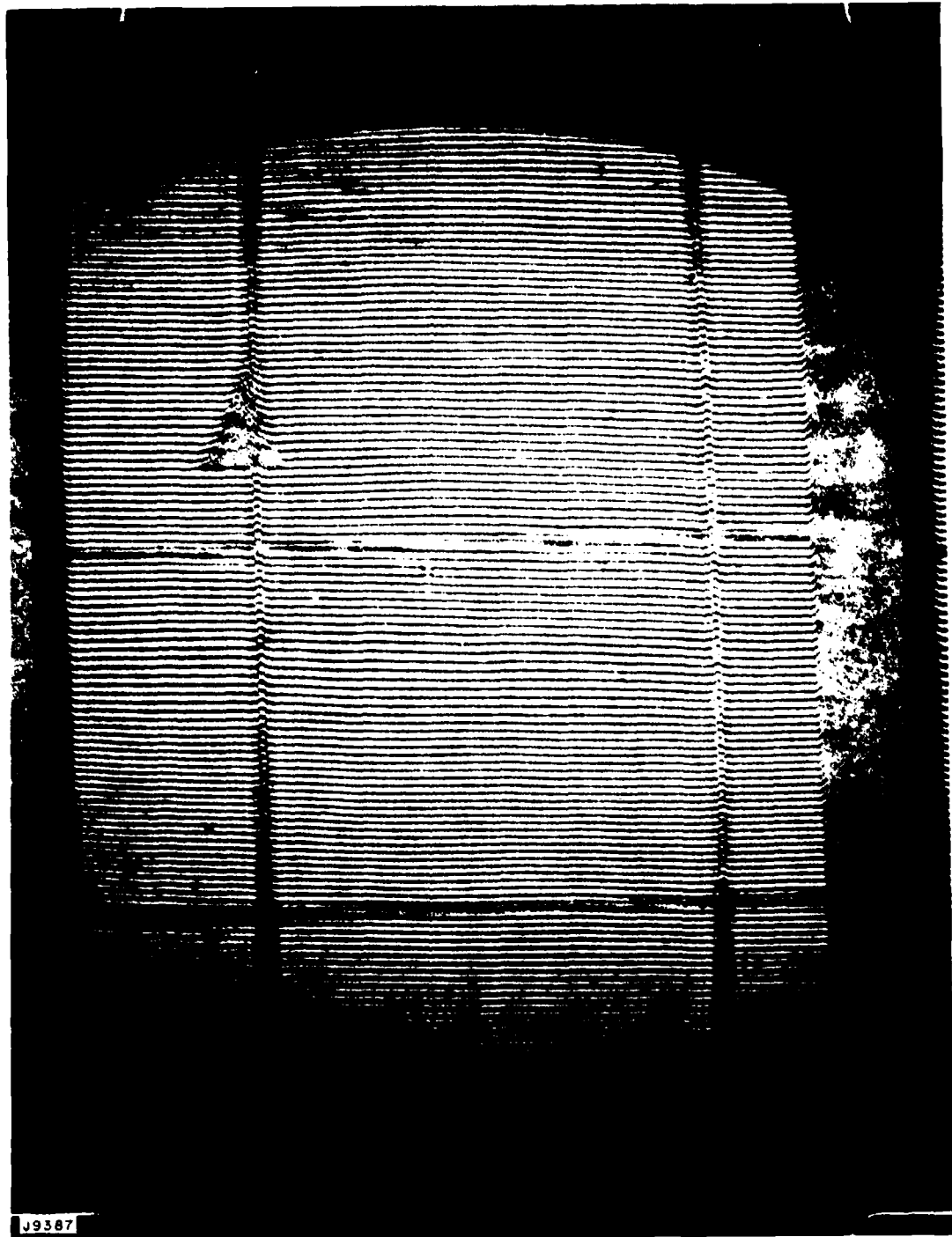


Figure 34. Tare (No Flow) Shot for Comparison with Figure 33

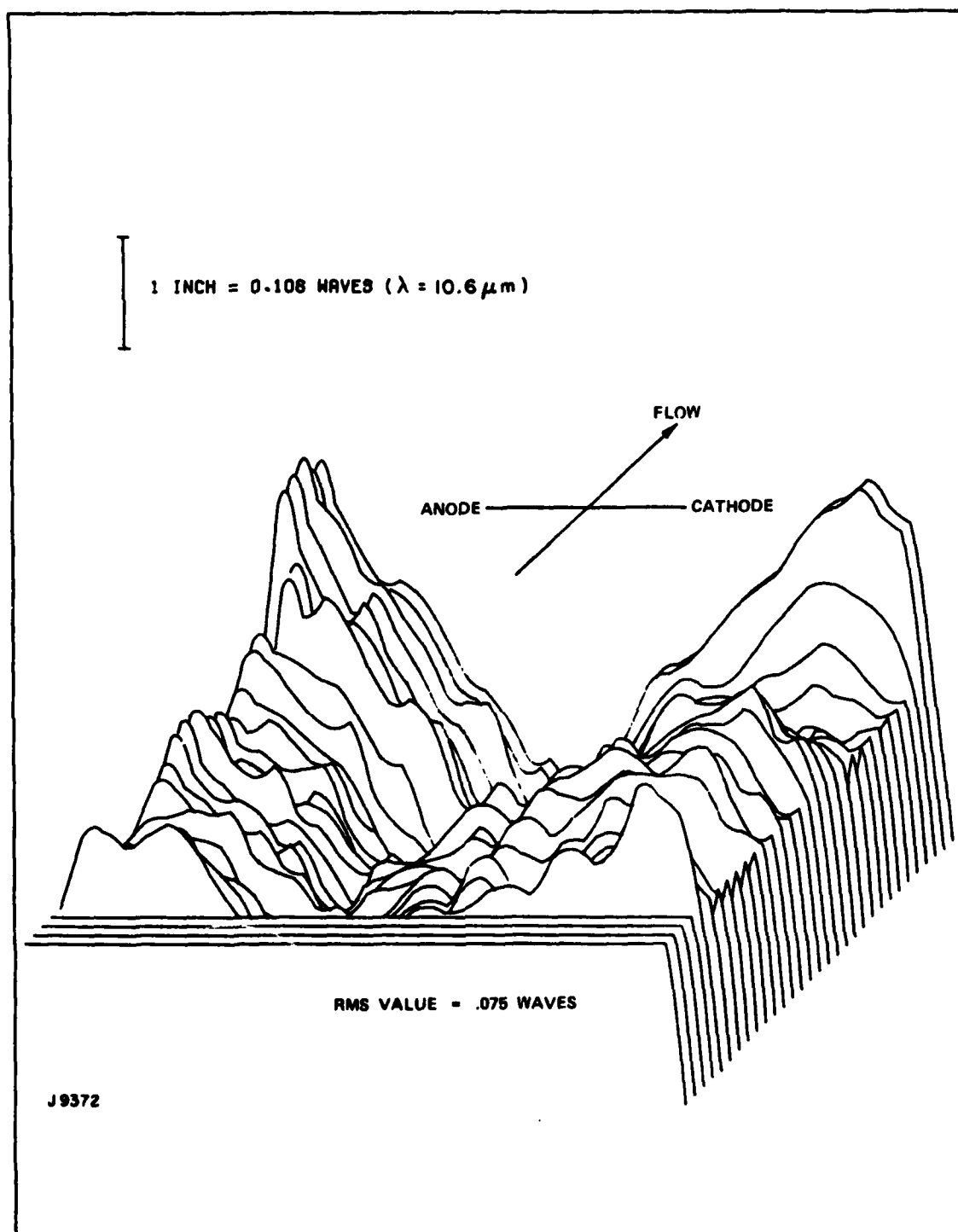


Figure 35. Near Field Phase Map from Interferogram Reduction;  
Only Tilt has been Removed

is of scale size  $(27 \text{ cm} \times 0.66)/33 \approx 0.5 \text{ cm}$  while in the anode-cathode direction the number is  $12/33 \approx 0.3 \text{ cm}$ . Recalling the discussion of Section 4.1, this clearly is too coarse by at least a factor of 10 to resolve any sources of wide angle scatter. To specifically search for such sources, it would be necessary to adjust the interferometer to produce very tiny fringes (i.e.,  $\lesssim 0.1 \text{ mm}$ ) and analyze a restricted portion of the beam. Such micro-interferometry is a desirable objective for further work.

Analysis of Figure 33 using the USAF version of FRINGE produced, not surprisingly, similar results. That version of FRINGE works with fewer data points (400) and has a mandatory algorithm to pre-smooth the contours. (Thus, filtering some of the effects we are looking for!) In this case the reduction yielded 0.082 waves RMS total, allocated among the low order aberrations as before.

## 5.0 CONCLUSIONS AND SUMMARY

- 1) A new photography-based technique has been developed to accurately characterize in detail pulsed IR laser beams.
- 2) A representative beam quality data base was obtained for ABEL, though no device adjustment to optimize beam quality was attempted. The best focal spot energy distributions indicated an encircled-energy times-diffraction-limited number of  $\leq 1.25$  XDL. The apparent dominant aberration was astigmatism, whose source is unclear at this time, but which in any event is easily correctable.
- 3) Medium quality interferometry predicts a better beam (1.15 Strehl XDL) than was observed. The effects of distortions evident in the interferograms were probably masked by the astigmatism mentioned in 2).
- 4) The near-field-to-farfield energy delivery fraction for ABEL was measured as 60-65%. This fraction was essentially insensitive to changes in flow rate, energy loading, or resonator obscuration position.

## APPENDIX A

### THEORETICAL FOCAL SPOT PATTERNS

#### 1. SIMPLE RECTANGULAR APERTURE

From the scalar theory of diffraction<sup>(1)</sup> the farfield amplitude is found from the Fourier transform of the near-field amplitude distribution

$$U(x_0, y_0) = \frac{\exp(i k f)}{i \lambda f} \iint_{\Gamma} \exp \left[ - \frac{2 \pi i}{\lambda f} (x_0 x_1 + y_0 y_1) \right] \cdot U_{nf}(x_1, y_1) dx_1 dy_1 \quad (A1)$$

where  $f$  is the focal distance,  $x_0, y_0$  and  $x_1, y_1$  coordinates in the far and near-fields, and  $\Gamma$  the near-field aperture. Since we want the focal pattern of a perfect beam, the near-field amplitude distribution  $U_{nf}$  is taken as unity.

For a simple rectangular aperture of dimension  $D_x$  by  $D_y$ , Eq. (A1) integrates to

$$U(x_0, y_0) = \frac{D_x D_y}{\lambda f} \operatorname{sinc} \left( \frac{x_0}{\lambda f / D_x} \right) \operatorname{sinc} \left( \frac{y_0}{\lambda f / D_y} \right) \quad (A2)$$

where the "sinc" function is defined as

$$\operatorname{sinc} Q = \frac{\sin \pi Q}{\pi Q} \quad (A3)$$

Then the farfield intensity distribution  $I'$ , normalized to unity at its center, is

$$\begin{aligned} I'(x_0, y_0) &= \left( \frac{\lambda f}{D_x D_y} \right)^2 U(x_0, y_0) U^*(x_0, y_0) \\ &= \operatorname{sinc}^2 \left( \frac{x_0}{\lambda f / D_x} \right) \operatorname{sinc}^2 \left( \frac{y_0}{\lambda f / D_y} \right) \end{aligned} \quad (A4)$$

1. Goodman, J.W., Introduction to Fourier Optics (McGraw-Hill, 1968), Ch. 2.

## 2. RECTANGULAR APERTURE WITH RECTANGULAR OBSCURATION

Now we consider a rectangular resonator having an aperture with outer dimensions  $D_x$  and  $D_y$ , and an obscuration with dimensions  $d_x$  and  $d_y$ . The obscuration is displaced away from the central position by amounts  $\ell_x$  and  $\ell_y$ . The integration region  $\Gamma$  is the area bounded by the rectangular aperture on the outside and the obscuration on the inside.

Rather than integrate Eq. (A1) directly, we decompose it into simpler forms whose solutions may be written down immediately. If we ignore the central obscuration, the farfield amplitude pattern of the remaining rectangle is

$$U(\text{outer}) = \frac{D_x D_y}{\lambda f} \operatorname{sinc} \left( \frac{x_0}{\lambda f / D_x} \right) \operatorname{sinc} \left( \frac{y_0}{\lambda f / D_y} \right) \quad (\text{A5})$$

The obscuration constitutes a "negative aperture" and by Babinet's Principle<sup>(2)</sup> its farfield is

$$U(\text{inner}) = - \frac{d_x d_y}{\lambda f} \operatorname{sinc} \left( \frac{x_0}{\lambda f / d_x} \right) \operatorname{sinc} \left( \frac{y_0}{\lambda f / d_y} \right) \quad (\text{A6})$$

if the observation coordinate system  $(x_0, y_0)$  is directly centered on the obscuration. If the obscuration is displaced, then the Fourier Shift Theorem (Goodman,<sup>(1)</sup> p. 9) says that the far-field amplitude is multiplied by an exponential

$$U_2(x_0, y_0) = - \exp \left[ - 2\pi i \left( \frac{x_0}{f \lambda / \ell_x} + \frac{y_0}{f \lambda / \ell_y} \right) \right] \quad (\text{A7})$$

. (previous expression)

The total amplitude  $U(x_0, y_0)$  is just  $U(\text{outer}) + U(\text{inner})$  and the intensity  $I(x_0, y_0)$  is again

$$I(x_0, y_0) = U(x_0, y_0) U^*(x_0, y_0) \quad (\text{A8})$$

2. Born, M. and Wolf, E., Principles of Optics, 5th Ed. (Pergamon, 1975), p 381.



If we define:

$$\frac{D_x}{d_x} = \frac{D_y}{d_y} \equiv M$$

$$\frac{\lambda_x}{D_x} = \frac{\lambda_y}{D_y} \equiv \epsilon$$

(This confined the obscuration to be centered along a diagonal of the resonator.) then we have, after some algebraic simplification, our final result

$$\begin{aligned} I'(x_0, y_0) &= \frac{I(x_0, y_0)}{\left[ \frac{M^2 - 1}{M^2} \left( \frac{D_x D_y}{\lambda z} \right) \right]^2} \quad (A9) \\ &= \left\{ \text{sinc}^2 x_0 \text{sinc}^2 y_0 + \frac{1}{M^4} \text{sinc}^2 \left( \frac{x_0}{M} \right) \text{sinc}^2 \left( \frac{y_0}{M} \right) \right. \\ &\quad \left. - \frac{2}{M^2} \text{sinc} x_0 \text{sinc} \frac{x_0}{M} \text{sinc} y_0 \text{sinc} \frac{y_0}{M} \cos[2\pi\epsilon(x_0 + y_0)] \right\} \\ &\quad \cdot \left\{ \frac{M^2}{M^2 - 1} \right\}^2 \end{aligned}$$

$I'$  is normalized to unit intensity at the center,  $x_0 = y_0 = 0$ , with the normalized farfield coordinates given by

$$x_0 = \frac{x_0}{f\lambda/D_x} \quad (A10)$$

$$y_0 = \frac{y_0}{f\lambda/D_y}$$

In all this work, we assume spatial uniformity in time throughout the laser pulse, so that the fluence distributions  $F(X_0Y_0)$  in  $J/cm^2$  are directly proportional to the intensity distributions.

## APPENDIX B

### COMPARISON OF TIMES-DIFFRACTION-LIMITED NUMBERS FOR BEAMS WITH ASTIGMATISM

We calculate here the case of astigmatism in beams of uniform intensity distribution defined by a square aperture.

The phase aberration is given by

$$\exp \left[ 2\pi i \frac{L}{2\lambda a^2} (x^2 - y^2) \right] \quad (B1)$$

where the area of the near-field aperture is  $4a^2$ , and  $L$  represents the peak to peak wave deformation of the astigmatism wavefront. The RMS value is given by

$$\phi_{\text{RMS}} = \phi_{\text{P-P}} / 2 \sqrt{6} = L / 2 \sqrt{6} \quad (B2)$$

The farfield amplitude distribution is just the Fourier transform of the phase aberration

$$U'(f_x, f_y) = \frac{1}{4a^2} \int_{-a}^{+a} \int_{-a}^{+a} \exp \left[ 2\pi i \left( f_x x + f_y y + \frac{L}{2\lambda a^2} [x^2 - y^2] \right) \right] dx dy \quad (B3)$$

If we define  $2L/\lambda \equiv \gamma^2$  and complete the square we have

$$U'(f_x, f_y) = \frac{1}{4a^2} \exp \left[ \frac{-2\pi i}{4} \frac{a^2}{\gamma^2} (f_x^2 - f_y^2) \right] \int_{-a}^{+a} \int_{-a}^{+a} \exp \left[ 2\pi i \frac{\gamma^2}{a^2} \left\{ \left( x + \frac{f_x a^2}{2\gamma^2} \right)^2 - \left( y - \frac{f_y a^2}{2\gamma^2} \right)^2 \right\} \right] dx dy \quad (B4)$$

Then we define

$$\begin{aligned} u &= \frac{2\gamma}{a} \left[ x + \frac{f_x}{2\gamma^2} a^2 \right] \\ v &= \frac{2\gamma}{a} \left[ y - \frac{f_y}{2\gamma^2} a^2 \right] \end{aligned} \quad (B5)$$

which leads to the form

$$\begin{aligned} U(f_x, f_y) &= \frac{1}{4\gamma^2} \exp \left[ -\frac{\pi}{2} i \frac{4a^2}{\gamma^2} \left( f_x^2 - f_y^2 \right) \right] \\ &\cdot \int_{-\gamma + (2f_x a/\gamma)}^{+\gamma + (2f_x a/\gamma)} du \int_{-\gamma - (2f_y a/\gamma)}^{+\gamma - (2f_y a/\gamma)} dv \\ &\cdot \exp \left[ i \frac{\pi}{2} (u^2 - v^2) \right] \end{aligned} \quad (B6)$$

This integral may be expressed in terms of Fresnel integrals

$$C(x) = \int_0^x \cos \frac{\pi}{2} t^2 dt \quad (B7)$$

$$S(x) = \int_0^x \sin \frac{\pi}{2} t^2 dt$$

Also, we note that the first zero of the theoretical (no aberration) pattern occurs at  $2 f_x a = 1 = 2 f_y a$ . Thus a normalized farfield coordinate

$$\begin{aligned} X &= 2 f_x a \\ Y &= 2 f_y a \end{aligned} \quad (B8)$$

may be employed. The final expression for the farfield amplitude function is then

$$U'(X,Y) = \frac{1}{4\gamma^2} \left\{ C \left[ \gamma + \frac{X}{\gamma} \right] + iS \left[ \gamma + \frac{X}{\gamma} \right] - C \left[ -\gamma + \frac{X}{\gamma} \right] - iS \left[ -\gamma + \frac{X}{\gamma} \right] \right\} \quad (B9)$$

$$\cdot \left\{ C \left[ \gamma + \frac{Y}{\gamma} \right] - iS \left[ \gamma - \frac{Y}{\gamma} \right] + C \left[ \gamma + \frac{Y}{\gamma} \right] - iS \left[ \gamma + \frac{Y}{\gamma} \right] \right\}$$

and, of course,

$$I'(X,Y) = U'[U']^*, \quad (B10)$$

The Strehl ratio is obtained when  $X = Y = 0$ :

$$SR = \frac{1}{\gamma^4} [C^2(\gamma) + S^2(\gamma)]^2 \cong \exp \left[ -\left( \frac{\pi L}{\lambda \sqrt{6}} \right)^2 \right] \quad (B11)$$

The unaberrated farfield amplitude is the well-known "sinc" function,  $(\sin \pi x)/\pi x$ :

$$U(f_x, f_y) = \frac{\sin 2\pi f_x a}{2\pi f_x a} \cdot \frac{\sin 2\pi f_y a}{2\pi f_y a} \quad (B12)$$

$$= \frac{\sin \pi X}{\pi X} \cdot \frac{\sin \pi Y}{\pi Y}$$

with

$$I(X,Y) = \left( \frac{\sin \pi X}{\pi X} \right)^2 \left( \frac{\sin \pi Y}{\pi Y} \right)^2 \quad (B13)$$

The Strehl ratio XDL is found from Eq. (B11) as  $(SR)^{-1/2}$ . To calculate the encircled energy XDL, we integrate Eqs. (B13) and (B10) out to  $|X| = |Y| = 1.0$  and take the square root of the ratio.

The results are shown on Figure B1. It is apparent that the Strehl ratio XDL is essentially the square of the encircled energy XDL for this case.

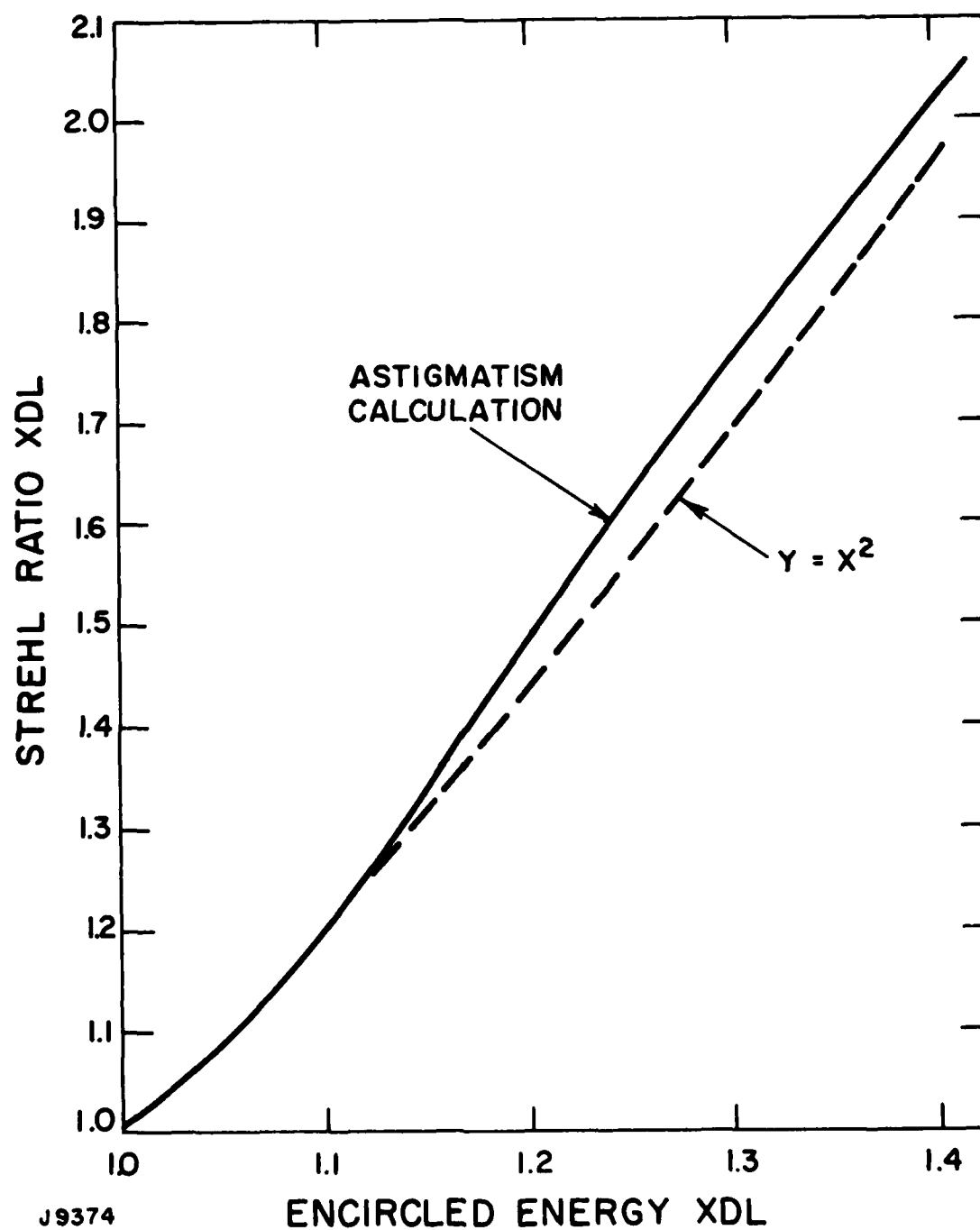


Figure B1. For Astigmatism, the Strehl XDL is Nearly the Square of the Encircled Energy XDL

DISTRIBUTION LIST

Commander US Army Missile Command Redstone Arsenal, AL 35898 Attn: DRSMI-RHB, Dr. T.A. Roberts RHE, Mr. J.C. Walters RHC, Mr. K. Smith RHC, Mr. Myron Cole RHS, Dr. George Dezenberg	10 copies
Commander US Army Mobility Equipment R&D Command Ft. Belvoir, VA 22060 Attn: DRDME-R, Mr. Cooper EA, Dr. Larry Amstutz	2 copies
Defense Advanced Research Projects Agency 1400 Wilson Boulevard Arlington, VA 22209 Attn: Director, Laser Division	1 copy
Air Force Weapons Lab Kirtland AFB, NM 87117 Attn: AFWL/ARAY, LTC T. Meyer	6 copies
Defense Documentation Center Cameron Station Alexandria, VA 22314	12 copies
RSIC Redstone Arsenal, AL 35898	3 copies

**END**

**FILMED**

**6-83**

**DTIC**